NH_3 decomposition for H_2 production by thermal and plasma catalysis using bimetallic catalysts

Shengyan Meng[a], Shangkun Li[a], Shuaiqi Sun[a], Annemie Bogaerts[b], Yi Liu[a]*, Yanhui Yi[a]*

[a] State Key Laboratory of Fine Chemicals, School of Chemical Engineering, Dalian University of Technology, Dalian 116024, Liaoning, China.

[b] Research group PLASMANT, Department of Chemistry, University of Antwerp, Universiteitsplein 1, BE-2610 Wilrijk-Antwerp, Belgium.

* Corresponding author: Prof. Dr. Yi Liu, Prof. Dr. Yanhui Yi

E-mail address: diligenliu@dlut.edu.cn, yiyanhui@dlut.edu.cn

ABSTRACT: Plasma catalysis has emerged as a promising approach for driving thermodynamically unfavorable chemical reactions. Nevertheless, comprehending the mechanisms involved remains a challenge, leading to uncertainty about whether the optimal catalyst in plasma catalysis aligns with that in thermal catalysis. In this research, we explore this question by studying monometallic catalysts (Fe, Co, Ni and Mo) and bimetallic catalysts (Fe-Co, Mo-Co, Fe-Ni and Mo-Ni) in both thermal catalytic and plasma catalytic NH_3 decomposition. Our findings reveal that the Fe-Co bimetallic catalyst exhibits the highest activity in thermal catalysis, the Fe-Ni bimetallic catalyst outperforms others in plasma catalysis, indicating a discrepancy between the optimal catalysts for the two catalytic modes in NH_3 decomposition. Comprehensive catalyst characterization, kinetic analysis, temperature program surface reaction experiments and plasma diagnosis are employed to discuss the key factors influencing NH_3 decomposition performance.

KEY WORDS: Hydrogen Energy; Ammonia Decomposition; Plasma Catalysis; Thermal Catalysis; Bimetallic Alloy Catalysts

1. Introduction

Non-thermal plasma (NTP), characterized by thermal non-equilibrium, provides a unique pathway to drive thermodynamically unfavorable chemical reactions at low temperatures (Bogaerts et al., 2020; Mehta et al., 2019; Neyts et al., 2015; Xu et al., 2023). Plasma catalysis, the combination of catalyst and plasma technology, exhibits catalyst-plasma synergistic effects. Plasma catalysis has been widely applied to activate and convert stable molecules (e.g., CO_2, N_2, CH_4) for energy and environmental applications (Cui et al., 2022; Meng et al., 2023; Wang et al., 2022; Wang et al., 2023). However, it is still uncertain whether the optimal catalyst in plasma catalysis aligns with that in thermal catalysis. Addressing this question is crucial for understanding the plasma-catalyst synergy and developing efficient catalysts for specific chemical reactions under plasma catalysis.

Hydrogen production through ammonia (NH_3) decomposition has received significant attention in recent years due to its exceptional qualities as a hydrogen carrier (Adamou et al., 2023; Lucentini et al., 2021; Sun et al., 2022). Although Ru has been acknowledged as the most active catalyst, its limited availability and high cost hinder large-scale applications (Chen et al., 2021; Fang et al., 2022). As a result, extensive research has been conducted on various non-noble metals, including Fe (Lu et al., 2010; Zhang et al., 2018), Ni (Kurtoglu et al., 2018; Qiu et al., 2022), and Co (Gu et al., 2015; Li et al., 2022), as well as transition metal carbide and nitride catalysts (Guo et al., 2015; Zheng et al., 2013), for NH_3 decomposition. The state-of-the-art results on NH_3 decomposition through conventional thermal catalysis have been listed in Table S1. Despite the progress, the recombinative desorption of the adsorbed nitrogen atoms (N_{ad}) on the non-noble metal surfaces remains challenging, which results in a lower NH_3 decomposition activity, unless the reaction is conducted at elevated temperature ($\geq$ ca. 550 ^{o}C) (Bell and Torrente-Murciano 2016). The thermodynamic equilibrium conversion of NH_3 in relation to reaction temperature at atmospheric pressure is shown in Figure 1, calculated using thermodynamic parameters

of NH_3, N_2 and H_2 molecules. NH_3 decomposition benefits from favorable thermodynamics, resulting in equilibrium conversions of 85.0%, 93.5%, 97.0%, 98.5% and 99.2% at 300 °C, 350 °C, 400 °C, 450 °C and 500 °C, respectively. However, the current NH_3 conversion achieved over non-noble metal catalysts remains significantly lower than the equilibrium conversion, especially under low temperature and high space velocity conditions, attributed mainly to kinetic blocking. In other words, there is a substantial potential to enhance the low-temperature performance of non-noble metal catalysts in NH_3 decomposition through a rational catalyst design approach.

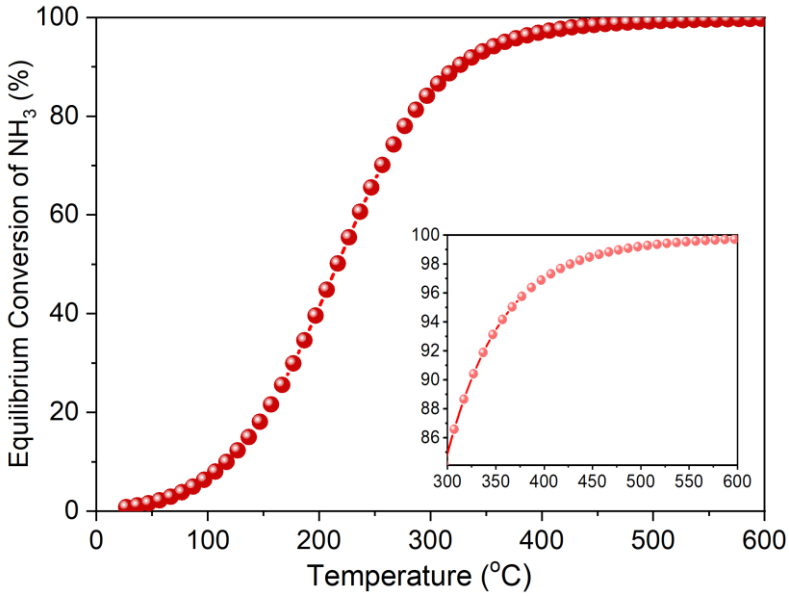

Figure 1. Thermodynamic equilibrium conversion of NH_3 into H_2 and N_2 at standard atmospheric pressure as a function of temperature. (100% NH_3 feed gas)

To improve the activity of non-noble metals at low temperatures, bimetallic alloys have become a pivotal strategy (Sun et al., 2022). Combining a metal with low metal-N binding energy (Ni and Co) and another metal with high metal-N binding energy (Fe and Mo) may result in a bimetallic catalyst with a moderate metal-N binding energy similar to that of Ru, ultimately enhancing non-noble metals' performance in NH_3 decomposition. Therefore, bimetallic catalysts, i.e., Fe-Ni (Silva et al., 2015; Simonsen et al., 2012), Fe-Co (Lendzion-Bielun and Arabczyk 2013; Zhang et al., 2008), Mo-Co (Srifa et al., 2016), and Co-Re (Kirste et al., 2021) have been studied in NH_3 decomposition. Another strategy

to improve the activity of non-noble metal catalysts in this process is through plasma catalysis. Previous papers reported a significant synergistic effect between dielectric barrier discharge (DBD) plasma and supported catalysts (Fe, Co, Ni and Cu) (Mukherjee et al., 2018; Wang et al., 2017; Wang et al., 2015; Wang et al., 2013; Yi et al., 2019).

In this paper, we report that among all the investigated catalysts (Fe, Co, Ni, Mo, as well as Fe-Co, Fe-Ni, Mo-Ni and Mo-Co bimetallic catalysts), the Fe-Co bimetallic catalyst exhibits the highest activity in thermal catalysis, while the Fe-Ni bimetallic catalyst shows the best activity in plasma catalysis. Hence, the optimal catalyst for NH_3 decomposition in thermal and plasma catalytic conditions is not the same. Moreover, catalyst characterization, kinetic analysis, and in-situ diagnostics were conducted to understand the reasons behind the suitability of Fe-Co and Fe-Ni catalysts for thermal catalytic and plasma catalytic NH_3 decomposition, respectively.

2. Experimental section

2.1 Catalyst Preparation

SiO_2 has been widely used as an "inert" catalyst support due to its low cost and excellent durability (Zhang et al., 2022). In our previous research, various materials with different relative dielectric constants (ε_d) were explored as potential catalyst supports, and SiO_2 was emerged as the preferred choice (Wang et al., 2015). The monometallic catalysts (Fe, Co, Ni and Mo), bimetallic catalysts (Fe-Co, Mo-Co, Fe-Ni and Mo-Ni) with a 5:5 metal molar ratio, and the Fe-Co bimetallic catalysts with varying Fe/Co molar ratios were prepared by the incipient-wetness impregnation method, using fumed SiO_2 as support. The detail preparation procedure is shown in Supplementary Information.

2.2 Activity Test

The experimental setup for the NH_3 decomposition activity test is shown in Figure S1. The temperature of the reactor wall was continuously monitored in situ using a thermocouple, while the

temperature of the catalyst bed was calibrated through FLIR equipment (Figure S2-S3). The exhaust gas was analyzed using an online gas chromatograph (GC) equipped with a thermal conductivity detector. During the reaction process, only H_2 and N_2 were produced, corresponding to a 100% mass balance.

$$X_{NH_3} = \frac{2Y}{1-2Y} \times 100\% \quad (1)$$

$$Q = X_{NH_3(p-c)} - (X_{NH_3(p)} + X_{NH_3(c)}) \quad (2)$$

The flow rate of NH_3 was precisely controlled at 120 ml/min using a mass flow controller. The NH_3 conversion was measured using an external standard method, and the conversion (X_{NH3}) is defined by equation 1, where Y represents the volume fraction of N_2, which was measured by GC. The accuracy of N_2 content is ensured by employing three different standard curve formulas ($Y_1 \leq 5\%$, $5\% < Y_2 \leq 15\%$, $15\% < Y_3 \leq 25\%$). The synergistic capacity (Q) between a catalyst and a DBD plasma is defined by equation 2, where $X_{NH3(p-c)}$, $X_{NH3(p)}$ and $X_{NH3(c)}$ correspond to the NH_3 conversion in "plasma + catalyst", "plasma alone" and "catalyst alone", respectively.

2.3 Catalyst Characterization and Plasma Diagnostics

The crystalline structure of the samples was analyzed using an X-ray diffractometer (XRD) with Cu Kα radiation (λ = 0.15406 nm). The hydrogen temperature-programmed reduction (H_2-TPR) of the samples (oxidation state) was examined using a ChemBET Pulsar chemical adsorbent. X-ray photoelectron spectroscopy (XPS) was conducted using Thermo Fisher ESCALAB XI+ with Al Kα X-ray source, and C 1s binding energy value (284.8 eV) was taken as a reference to calibrate the binding energy. Metal loadings were measured using X-ray fluorescence (XRF). The morphology and particle size of the catalysts were examined with high resolution transmission electron microscopy (HRTEM) and high-angle annular dark-field scanning transmission electron microscopy (HAADF-STEM), respectively, while energy-dispersive X-ray (EDX) spectrometry was used to analyze the chemical composition of the catalysts. The specific surface area, total pore volume, and pore diameter of the

samples were measured using N_2 physisorption. To Characterize acidity and NH_3 adsorption-desorption property, ammonia temperature programmed desorption (NH_3-TPD) of the samples was carried out with ChemBET Pulsar Chemical Adsorbent, while quantifying active sites for NH_3 chemisorption was achieved by titration. The NH_3 plasmas (in the presence and absence of catalysts) were diagnosed using optical emission spectra (OES). The detailed instrument information and specific operating parameters are shown in Supplementary Information.

3. Results

3.1 Thermal Catalytic NH_3 Decomposition Activity

Figure 2A depicts the NH_3 conversion of the Fe, Co, Ni, Mo, Fe-Co, Mo-Co, Fe-Ni and Mo-Ni catalysts under thermal catalysis. It is evident that the Fe-Co catalyst exhibits superior activity compared to the other catalysts. Furthermore, Fe-Co bimetallic catalysts with varying Fe/Co molar ratios (constant total loading of 10 wt.%) were evaluated under the same conditions (Figure 2B). Notably, the optimal Fe/Co molar ratio is approximately 1/1 (i.e., 5Fe-5Co). With the use of the 5Fe-5Co catalyst, NH_3 was nearly completely decomposed (> 99.5%) at 585 ^oC. As shown in Figure 2C, the 5Fe-5Co catalyst was continuously tested for 100 hours, with the temperature alternating between 560 and 585 ^oC, and NH_3 conversion fluctuating between 73% and 99.6%, respectively. These results establish Fe-Co bimetallic catalyst as the optimal choice for thermal catalytic NH_3 decomposition, offering excellent catalytic stability.

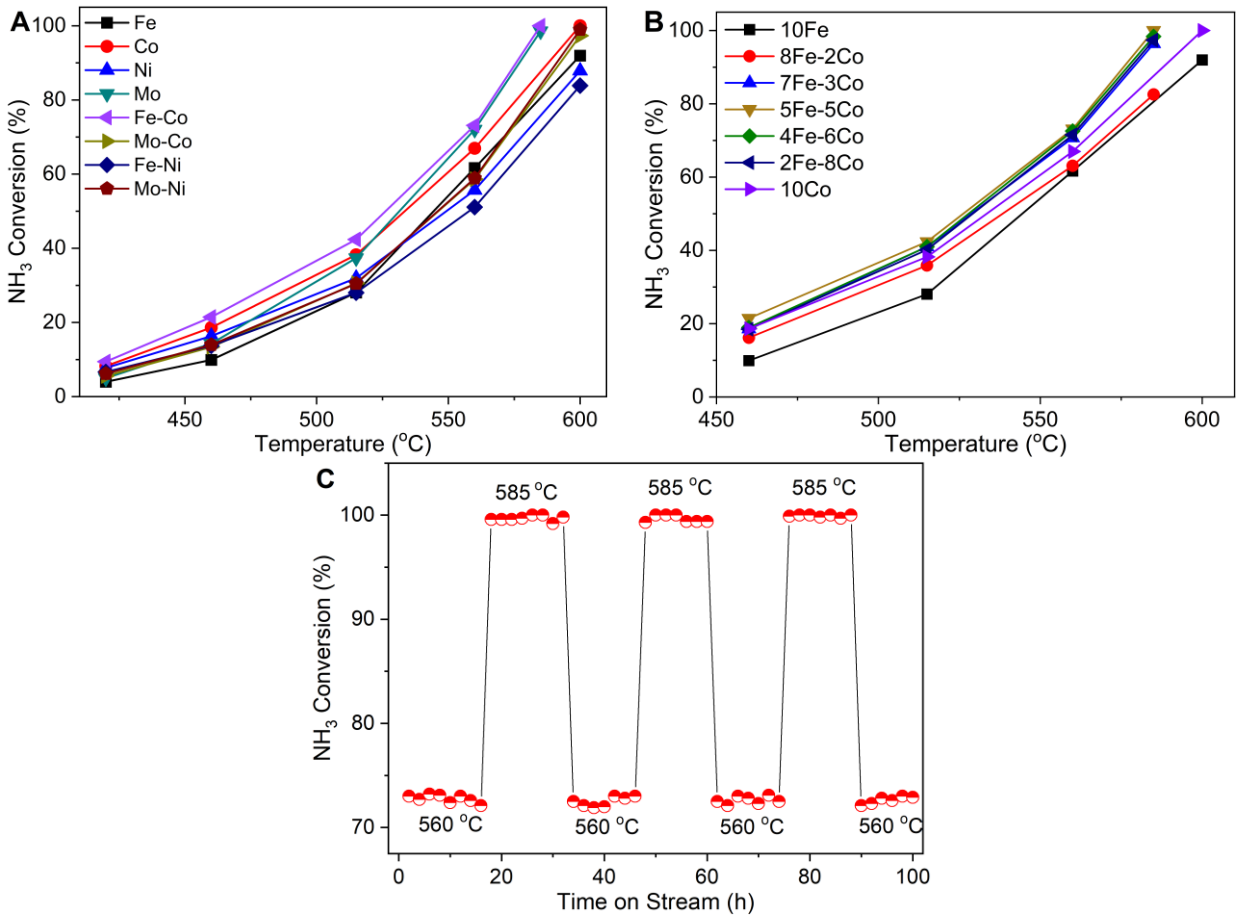

Figure 2. **Results of thermal catalytic NH_3 decomposition**. (A) Fe, Co, Ni, Mo, Fe-Co, Mo-Co, Fe-Ni and Mo-Ni catalysts; (B) Fe-Co bimetallic catalysts with varying Fe/Co molar ratios; (C) Stability performance of 5Fe-5Co catalyst. (0.5 g catalyst, 120 ml/min NH_3, 14400 h^{-1} space velocity, 3 mm discharge gap, 10 kHz discharge frequency)

3.2 Plasma Catalytic NH_3 Decomposition Activity

In Figure 3A, the Fe-Ni catalyst exhibits the highest activity, achieving approximately 60% NH_3 conversion, compared to other catalysts under plasma catalysis conditions, even at a relatively low temperature of 460 °C (570 °C without plasma). Detailed reaction conditions and NH_3 conversion for both "plasma alone" and "catalyst alone" are shown in Table S2. The synergistic capacity of the catalysts in plasma catalytic NH_3 decomposition was calculated using equation 2 (Figure 3B). It is evident that Fe-Ni bimetallic catalysts (i.e., 5Fe-5Ni) exhibit the strongest plasma-catalyst synergistic capacity. These results indicate that the Fe-Ni bimetallic catalyst is the optimal catalyst in plasma catalytic NH_3 decomposition for H_2 production.

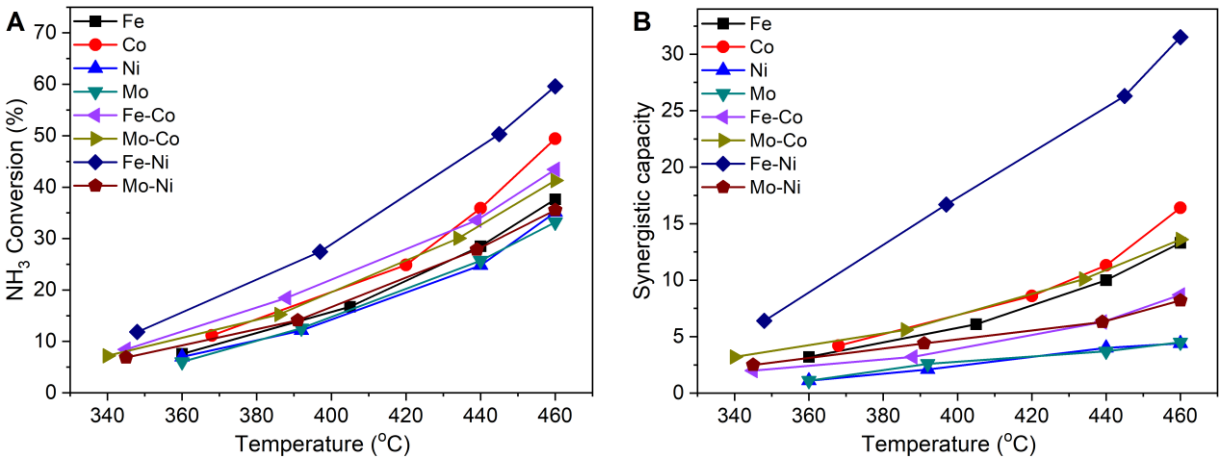

Figure 3. Results of plasma catalytic NH_3 decomposition over Fe, Co, Ni, Mo, Fe-Co, Mo-Co, Fe-Ni and Mo-Ni catalysts. (A) NH_3 conversion; (B) Synergistic capacity. (0.5 g catalyst, 120 ml/min NH_3, 14400 h^{-1} space velocity, 3 mm discharge gap, 10 kHz discharge frequency).

3.3 Physicochemical Properties of the Catalysts

In plasma catalytic NH_3 decomposition, the phase states of the fresh and spent catalysts (Fe, Co, Ni, Mo, Fe-Co, Mo-Co, Fe-Ni and Mo-Ni) are shown in Figures S4-S7. The phase states of the fresh catalysts were dominated by Fe_2O_3, Co_3O_4, NiO and MoO_3. However, they transformed into the crystalline phases of Ni, Fe_2N, Mo_2N and $Co_{5.47}N$, respectively, upon NH_3 decomposition. For the fresh Mo-Ni and Mo-Co bimetallic catalysts, "MoO_3 + NiO" and "MoO_3 + Co_3O_4" mixed crystals formed, transforming into "Mo_2N + Ni" and "Mo_2N + $Co_{5.47}N$", respectively, after the NH_3 decomposition. Interestingly, in the fresh Fe-Co and Fe-Ni bimetallic catalysts, spinel structures of $CoFe_2O_4$ and $NiFe_2O_4$ emerged, later converting into FeCo alloys and Fe_3NiN after the NH_3 decomposition. The XRD profiles of the bimetallic Fe-Co catalysts with varied Fe/Co ratios under thermal catalysis are shown in Figure S8. The Fe-Co bimetallic catalysts transformed from the initial $CoFe_2O_4$ spinel phase to FeCo alloy phase after undergoing NH_3 decomposition reaction. It should be mentioned that the final crystalline phase remains constant regardless of thermal or plasma catalysis NH_3 decomposition, indicating uniformity in the catalytically active phase.

The H_2-TPR profiles of 10Fe, 10Co and Fe-Co bimetallic catalysts with varying Fe/Co ratio are depicted in Figure 4. Clearly, the H_2-TPR profile of 10Fe catalyst shows four peaks at 412 ºC, 550 ºC, 677 ºC and 748 ºC, attributed to the reduction of $Fe_2O_3 \rightarrow Fe_3O_4$, $Fe_3O_4 \rightarrow FeO$, $FeO \rightarrow Fe$ and reduction of FeO species with strong interaction with the support, respectively. Likewise, the 10Co catalyst primarily shows three peaks at 340 ºC, 391 ºC and 445 ºC, associated with the reduction of $Co_3O_4 \rightarrow CoO$, $CoO \rightarrow Co$ and reduction of CoO species with strong interaction with the support, respectively. The H_2-TPR profile of the 5Fe-5Co catalyst displays four peaks at 379 ºC, 489 ºC, 580 ºC and 730 ºC, corresponding to the reduction of $CoFe_2O_4 \rightarrow Co\text{-}Fe_3O_4$, $Co\text{-}Fe_3O_4 \rightarrow Co\text{-}FeO$, $Co\text{-}FeO \rightarrow Co\text{-}Fe$, and the reduction of Co-FeO species with strong interaction with the support, respectively. Comparative analysis of 10Fe, 5Fe-5Co and 10Co samples (Figure 4B) indicates that the addition of Co lowers the reduction temperature of iron oxide. Furthermore, the H_2-TPR profile of 5Fe-5Co sample provides evidence for the formation of $CoFe_2O_4$ spinel phase, consistent with XRD results (Figure S8).

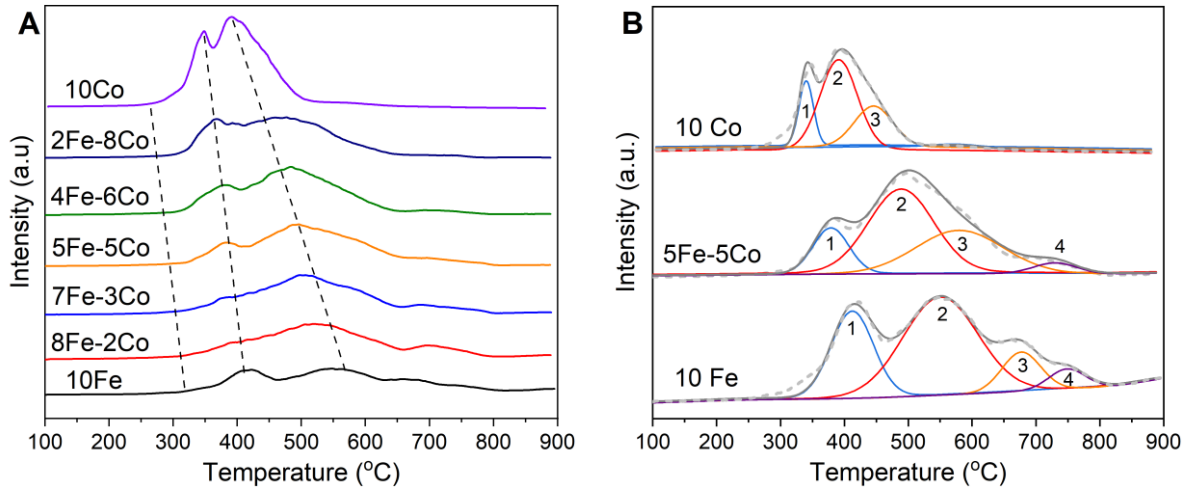

Figure 4. H_2-TPR results. (A) Fe-Co bimetallic catalysts with varying Fe/Co molar ratios; (B) The fitting peaks of H_2 consumption for 10Fe, 5Fe-5Co and 10Co catalysts.

The XPS profile the 10Fe, 10Co and Fe-Co bimetallic samples with varying Fe/Co ratio is shown in Figure 5. The Fe 2p core level XPS profile of the 10Fe and Fe-Co bimetallic samples reveals that the intensity of both $Fe2p_{3/2}$ (710.5 eV) and $Fe2p_{1/2}$ (724.5 eV) elevates with increasing Fe content (Figure

5A). Furthermore, the signal of Fe^{III} has been observed, suggesting the existence of Fe_2O_3 or $CoFe_2O_4$ phase, which is consistent with XRD and H_2-TPR results. In Figure 5B, the Co 2p core level XPS profile of the 10 Co and Fe-Co bimetallic samples with varying Fe/Co ratio is presented, in which the intensities of both $Co2p_{3/2}$ (779.7 eV) and $Co2p_{1/2}$ (795.8 eV) increase with higher Co content. It is worth mentioning that the main peaks of $Co2p_{3/2}$ (779.7 eV) and $Co2p_{1/2}$ (795.8 eV) for Co^{II} species are usually indistinguishable from those of Co^{III} species, respectively, making them inadequate for distinguishing between Co^{II} and Co^{III} species. However, the satellite peaks cannot be clearly identified, due to the low ratio of signal to noise. Therefore, regarding the 5Fe-5Co catalyst, XPS spectra show the presence of Fe^{III}, as well as Co^{II} or Co^{III}, while XRD and H_2-TPR results confirm the existence of $CoFe_2O_4$ spinel phase.

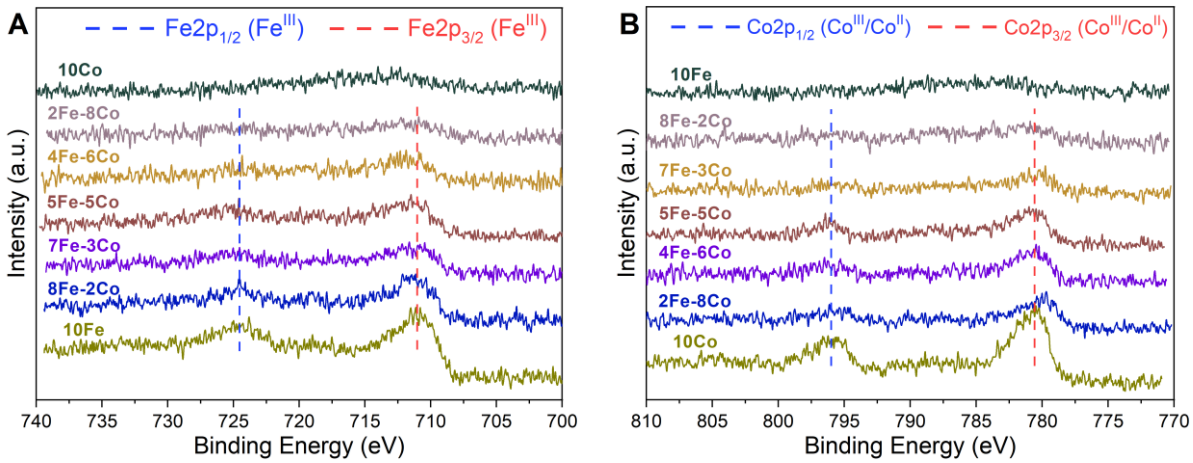

Figure 5. XPS profile of Fe, Co and Fe-Co bimetallic catalysts. (A) Fe 2p XPS results; (B) Co 2p XPS results.

The XRF results of the Fe, Co, Ni, Mo, Fe-Co, Mo-Co, Fe-Ni and Mo-Ni catalysts are shown in Tables S3-S4, while Tables S5-S6 present the XRF results for Fe-Co bimetallic catalysts with varying Fe/Co ratios. These results indicate that the actual loading is approximately 10 wt.% (ranging from 9.6 to 10.1 wt.%), which closely aligns with the calculated loading.

HRTEM images of the fresh catalysts are presented in Figure S9 and the particle size distributions are shown in Figure S10. The Co catalyst exhibits the smallest particle size, ranging from 3 to 8 nm,

while the Fe and Mo catalysts show particle sizes ranging from 10 to 16 nm and 8 to 20 nm, respectively. The Fe-Co and Fe-Ni catalysts fall within 4 to 20 nm, whereas the Mo-Co and Mo-Ni catalysts show relatively larger particles (10 to 100 nm and 5 to 500 nm, respectively).

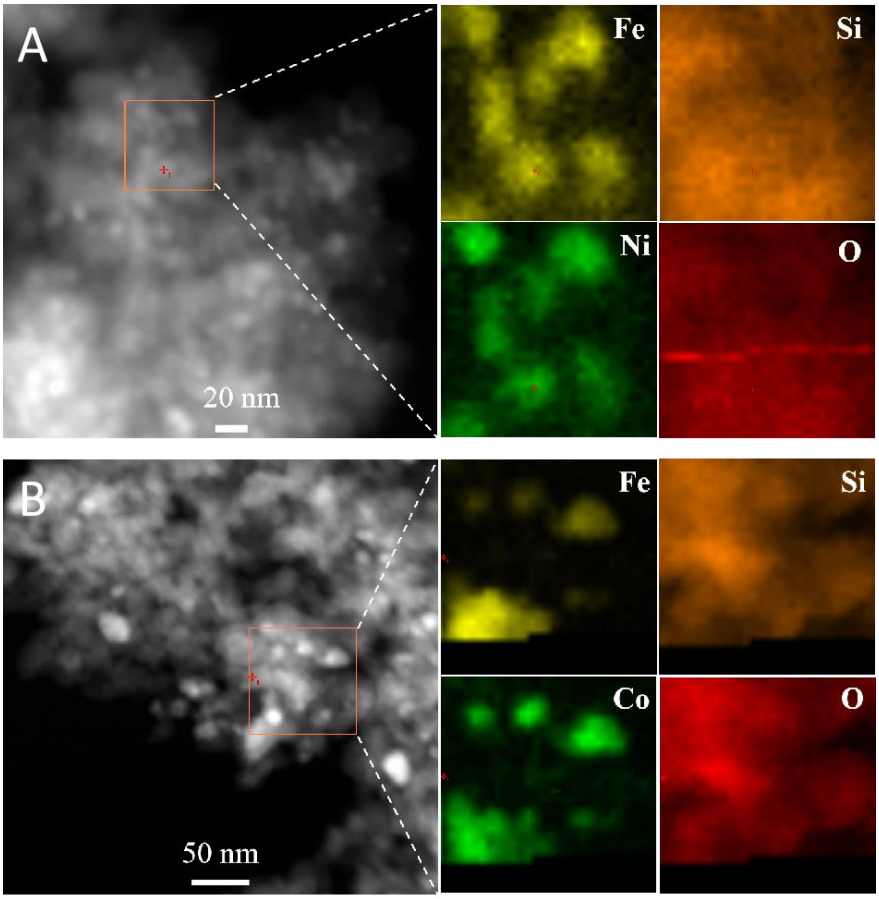

Figure 6. HAADF-STEM mapping images. (A) Fe-Co bimetallic catalysts (5Fe-5Co), (B) Fe-Ni bimetallic catalysts (5Fe-5Ni).

The distribution of elements in the spent bimetallic catalysts particles was investigated using HAADF-STEM and EDX spectrometry. Figure 6 illustrates that in the Fe-Co and Fe-Ni bimetallic catalysts, the corresponding metals are found at the same location in the scanning mapping images, indicating their combination. The line scanning results (Figures S11-S12) reveal synchronous variations in the content of the corresponding metals along the scanning line. These results provide additional evidence for the formation of FeCo alloys and Fe_3NiN, which aligns with the XRD results (Figures S7-

S8). Furthermore, the HAADF-STEM mapping images of Mo-Co and Mo-Ni catalysts are shown in Figures S13-S14.

The BET surface area, pore volume and average pore diameter were calculated for all the samples using N_2 adsorption-desorption isotherms (Tables S7−S8). The BET surface area and pore volume showed a slight decrease for the catalysts after loading with metals, which could be attributed to the impregnation of the precursor in the support pores. As for the BET surface area, pore volume and average pore diameter, no significant differences were observed among the prepared catalysts.

The NH_3-TPD was employed to characterize the NH_3 adsorption-desorption properties of the catalysts, as it is closely related to the catalytic performance, given NH_3's role as the reactant. Furthermore, in NH_3 decomposition reaction, the process is typically initiated by the chemisorption of NH_3 molecules on the catalysts surface. Consequently, NH_3-TPD provides indirect insights into the active sites rather than an accurate measurement.

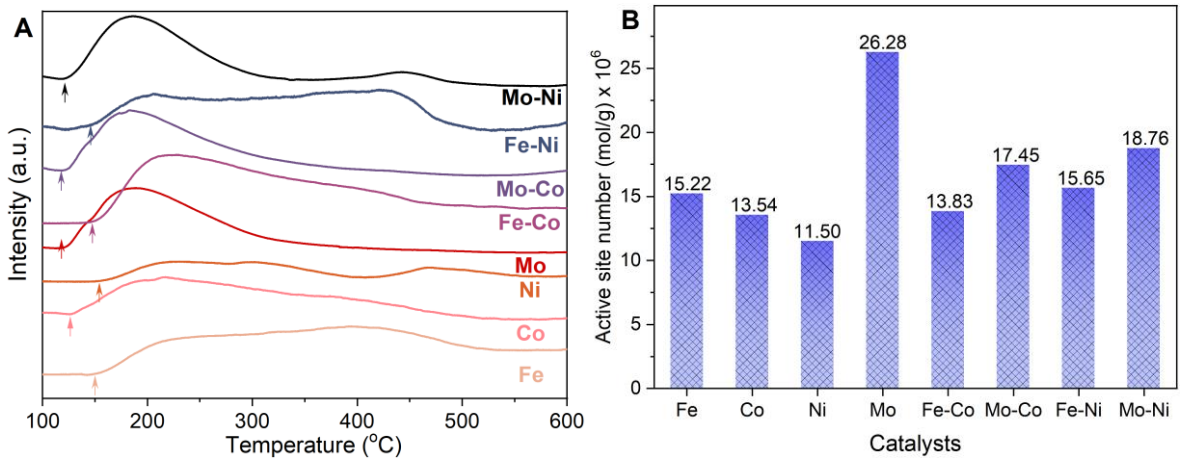

Figure 7. The (A) NH_3-TPD profiles and (B) NH_3 chemisorption active site numbers of the spent Fe, Co, Ni, Mo, Fe-Co, Mo-Co, Fe-Ni and Mo-Ni catalysts.

Figure 7A illustrates the NH_3-TPD profiles of the spent Fe, Co, Ni, Mo, Fe-Co, Mo-Co, Fe-Ni and Mo-Ni catalysts. The Fe and Ni monometallic catalysts exhibit weak chemisorption sites for NH_3 (desorbing at low temperatures, i.e., < 300 ºC), along with moderate chemisorption sites (300-400 ºC) and strong chemisorption sites (desorbing at high temperatures, i.e., > 400 ºC). However, the Co catalyst

shows some weak sites and a small part of moderate sites, while the Mo catalysts only display weak chemisorption sites. Among the bimetallic catalysts (Fe-Co, Mo-Co, Fe-Ni and Mo-Ni), the Fe-Ni and Fe-Co catalysts reveal abundant moderate sites, while the Mo-Ni catalysts exhibit numerous weak sites and a very small number of strong sites. Only weak sites are detected in Mo-Co catalysts. These results indicate that Fe-Co and Fe-Ni bimetallic catalysts exhibit a large number of moderate sites for NH_3 chemisorption, which could be attributed by the formation of FeCo alloy and Fe_3NiN phase. Furthermore, the number of the NH_3 chemisorption sites was measured indirectly through titration following the NH_3-TPD experiment, and the results are shown in Figure 7B. The active sites for NH_3 chemisorption over the Fe, Co, Ni, Mo, Fe-Co, Mo-Co, Fe-Ni and Mo-Ni catalysts are measured at 15.22, 13.54, 11.50, 26.28, 13.83, 17.45, 15.65 and 18.76 μmol/g, respectively.

4. Discussion

Figures 2-3 exhibit the superior performance of the Fe-Co bimetallic catalyst in thermal catalytic NH_3 decomposition, while the Fe-Ni bimetallic catalyst is the optimal catalyst in plasma catalysis. The N_2-physisorption results (Tables S7-S8) indicate a similar porosity among the prepared catalysts, including BET surface area, pore volume and pore diameter, suggesting that these factors do not determine the catalytic activity. In light of the diameters of the mesopores in the catalysts (> 12 nm), which significantly exceed the size of NH_3 molecules (0.326 nm), N_2 molecules (0.364 nm) and H_2 molecules (0.289 nm), it is plausible that mass transfer, specifically diffusion, may not serve as the limiting factor. Essential insights are provided by XRD, H_2-TPR, XPS, HRTEM and HAADF-STEM analyses. Integrating the above activity and characterization results, the high activity of the Fe-Co catalyst in thermal catalytic NH_3 decomposition is probably attributed to the FeCo alloy phase, while the exceptional performance of the Fe-Ni catalyst in plasma catalytic NH_3 decomposition may be caused by the Fe_3NiN phase.

4.1 Kinetic Analysis

To elucidate the superior activity of Fe-Co and Fe-Ni catalysts in thermal and plasma catalytic NH_3 decomposition, respectively, we conducted tests on above catalysts at a tenfold higher space velocity using both thermal and plasma catalysis. The elevated space velocity condition ensures NH_3 conversion remains below 20%, thereby eliminating the influence of surface coverage and gas phase composition on the reaction kinetics. The reason for choosing different temperature ranges (420-600 ºC for thermal and 360-460 ºC for plasma) is to ensure similar conversion degrees under thermal and plasma catalysis conditions. Consequently, the rate of NH_3 decomposition could be utilized to calculate the apparent activation energy (Ea) of the NH_3 decomposition reaction through the Arrhenius equation.

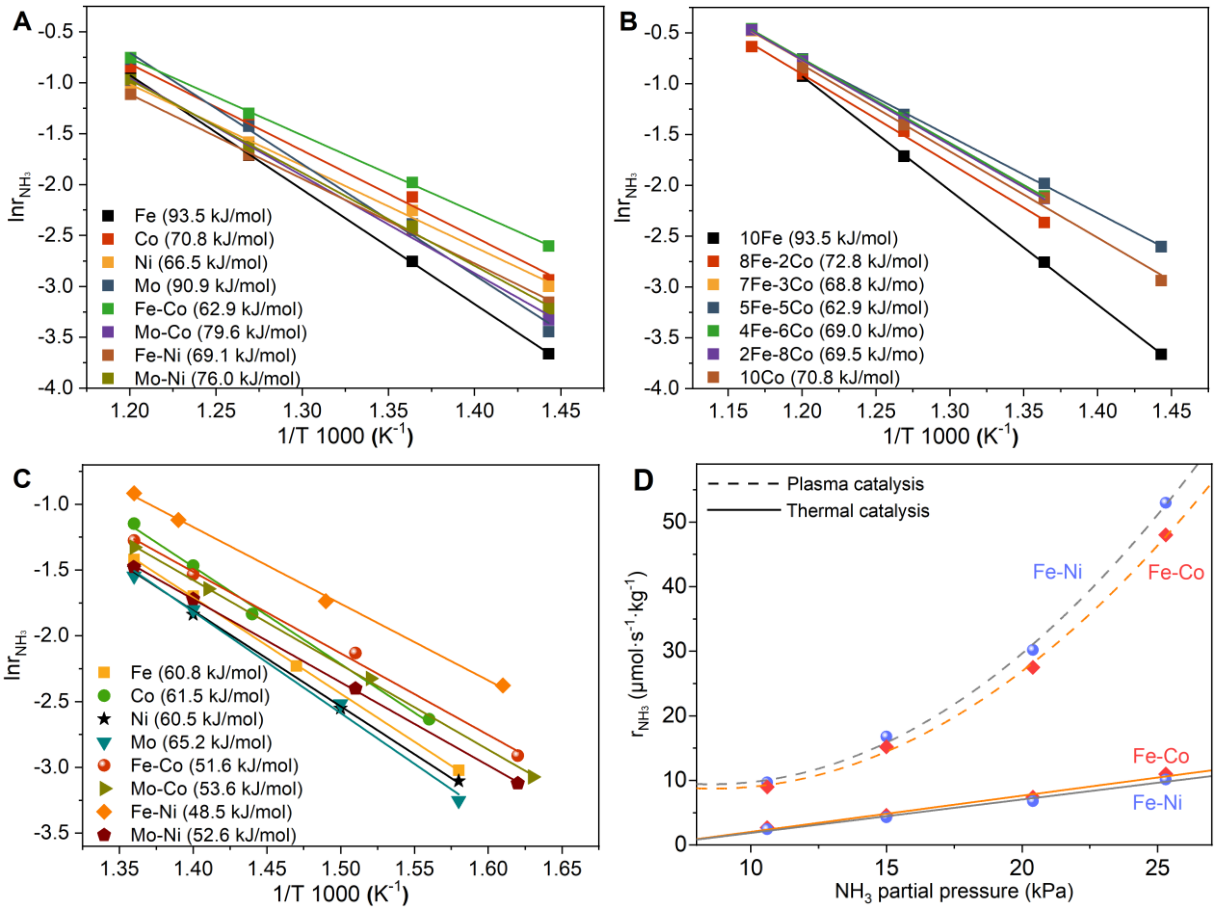

Figure 8. (A-C) Arrhenius plots. (A) Thermal catalytic NH_3 decomposition by Fe, Co, Ni, Mo, Fe-Co, Mo-Co, Fe-Ni and Mo-Ni catalysts; (B) Thermal catalytic NH_3 decomposition by Fe-Co bimetallic catalysts with varying Fe/Co molar ratios; (C) Plasma catalytic NH_3 decomposition over Fe, Co, Ni, Mo, Fe-Co, Mo-Co, Fe-Ni and Mo-Ni catalysts (0.5 g catalyst, 1200 ml/min NH_3, 144000 h^{-1} space velocity, NH_3 conversion was maintained below 10%). The apparent

activation energy is provided within brackets. (D) The variation of reaction rates with NH_3 partial pressure over Fe-Ni and Fe-Co catalysts (350 °C, Ar as the balance gas)

Figure 8A illustrates the Arrhenius plots of the Fe, Co, Ni, Mo, Fe-Co, Mo-Co, Fe-Ni and Mo-Ni catalysts in thermal catalytic NH_3 decomposition, while Figure 8B shows the Arrhenius plots of the Fe-Co bimetallic catalysts with varying Fe/Co ratio. Notably, the 5Fe-5Co catalyst exhibits the lowest Ea (Table 1) for thermal catalytic NH_3 decomposition. In plasma catalytic NH_3 decomposition, the Arrhenius plots of the Fe, Co, Ni, Mo, Fe-Co, Mo-Co, Fe-Ni and Mo-Ni catalysts are shown in Figure 8C, where the Fe-Ni catalyst exhibits the lowest Ea (Table 1). Based on the NH_3 decomposition rate (at 460 °C) and the number of active sites derived from the NH_3-TPD results (Figure 7), we calculated the turnover frequency (TOF) of the catalysts. Table 1 indicates that the Fe-Co catalyst exhibits the highest TOF for thermal catalytic NH_3 decomposition, and the TOFs of the catalysts follow the order Fe-Co > Ni > Co > Fe-Ni > Mo-Co > Mo-Ni > Fe, with the sequence of Ni > Co > Fe aligning with the literature results summarized in the most recent review (Mukherjee et al., 2018). The reaction rates of NH_3 decomposition were calculated as a function of its partial pressure, as shown in Figure 8D. In thermal catalysis, the NH_3 decomposition rate exhibited a linear relationship with its partial pressure, consistent with a first-order reaction. This observation confirms that NH_3 decomposition is indeed a first-order reaction under conventional thermal catalysis. However, under plasma catalysis conditions, the NH_3 consumption rate showed a non-linear relationship with its partial pressure, indicating that the reaction order may fall between first-order and second-order kinetics, suggesting a different reaction mechanism or rate limiting step in plasma-catalytic NH_3 decomposition.

This result strongly suggests that under plasma catalysis, the reaction mechanism and the steps controlling the reaction rate are different from those under thermal catalysis. Plasma catalysis likely allows for a more favorable set of conditions that enable alternative reaction pathways.

Table 1. Apparent activation energy and turnover frequency of NH_3 decomposition over the various catalysts under thermal and plasma catalysis.

Catalysts	Apparent activation energy (kJ/mol)		Turnover frequency (TOF; s^{-1}) [a]	
	Thermal catalysis	Plasma catalysis	Thermal catalysis	Plasma catalysis
Fe	93.5	60.8	1.16	2.73
Co	70.8	61.5	2.46	4.61
Ni	66.5	60.5	2.54	3.21
Mo	90.9	65.2	0.97	1.27
Fe-Co	62.9	51.6	2.77	3.75
Mo-Co	79.6	53.6	1.37	2.75
Fe-Ni	69.1	48.5	1.56	5.95
Mo-Ni	76.0	52.6	1.33	2.01

[a] the TOF value was calculated based on the reaction results at 460 °C, and the TOF of plasma catalysis has deducted the corresponding NH_3 conversion from plasma alone.

The Fe-Ni catalyst exhibits the highest TOF for plasma catalytic NH_3 decomposition, and Table 1 presents the kinetic data revealing two crucial phenomena. (i) The Ea of NH_3 decomposition under plasma catalysis is lower that than for thermal catalysis, suggesting that plasma reduces the Ea during NH_3 decomposition. (ii) The specific catalyst's TOF for NH_3 decomposition under plasma catalysis is significantly higher compared to thermal catalysis, indicating that the plasma enhances the rate of the catalytic cycling. In the case of Fe-Ni, a change in Ea of 20.6 kJ/mol according to the Arrhenius equation should result in a rate change of 30-fold. However, we only observed an approximately 4-fold increase in TOF and conversion. The main reason may be the difference in reaction mechanism and rate-limiting step (section 4.4). In thermal catalysis, the rate-limiting step is well-established as the recombination and desorption of adsorbed nitrogen species (N*). Plasma catalysis, however, involves a more intricate mechanism, and the exact nature of its rate-limiting step remains an ongoing area of research.

4.2 Strength of Metal-N Binding

To elucidate the reasons for the lowest Ea and the highest TOF in thermal catalytic NH_3 decomposition over Fe-Co catalysts, it is meaningful to clarify the mechanism of thermal catalytic NH_3 decomposition. In thermal catalysis, NH_3 molecules first adsorb on the catalyst surface, gradually dehydrogenate to form adsorbed NH_{2ad}, NH_{ad}, H_{ad} and N_{ad} species (Wang et al., 2015), and finally desorb from the catalyst surface through recombinative desorption (Langmuir-Hinshelwood mechanism) to produce H_2 and N_2.

We designed temperature program surface reaction (TPSR) experiments for further investigation. Initially, the fresh catalysts (metal oxide) were reduced to metals (or alloys) at 600 ºC through H_2 treatment, followed by purging with Ar flow at 450 ºC. Subsequently, continuous NH_3 feed was supplied for thermal catalytic NH_3 decomposition (450 ºC) over the samples for 1 hour. Afterward, the above samples were cooled to 250 ºC and maintained at this temperature for 1 hour under Ar atmosphere, resulting in abundant adsorbed N_{ad}, H_{ad}, NH_{ad}, NH_{2ad} and NH_{3ad} species on the surface of the catalysts. Finally, using a mass spectrometer (MS), we examined the desorption of N_2 and H_2 (in Ar atmosphere) with a temperature program ranging from 250 ºC to around 780 ºC at a heating rate of 10 ºC/min.

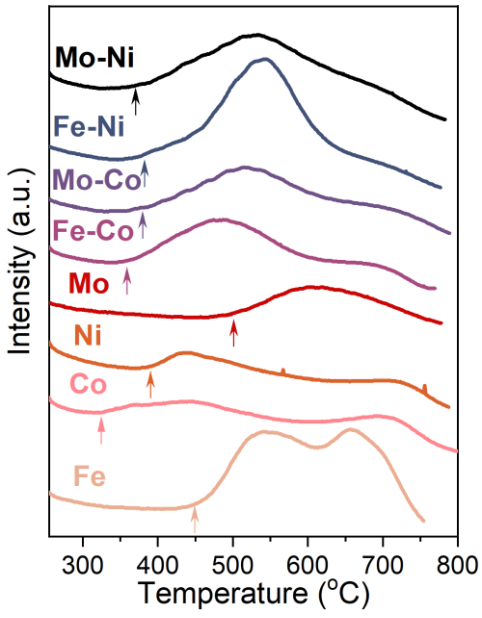

Figure 9. MS signal of N_2 formation during TPSR experiments.

The MS signal in Figure 9 exhibits the N_2 generation resulting from recombinative desorption reaction of adsorbed NH_{2ad}, NH_{ad} and N_{ad} species on the catalysts surface, and the accompanying signal of H_2 formation is exhibited in Figure S15. A comparison of the initial N_2 formation and desorption temperatures (indicated by arrows) between Mo and Fe catalysts (490 ºC and 450 ºC, respectively) and the surfaces of Co and Ni catalysts (335 ºC and 390 ºC, respectively) indicates varying M-N binding energies. Specifically, Mo and Fe catalysts display relatively strong M-N binding energies, whereas Co and Ni catalysts are relatively weak. This discrepancy leads to the easier recombinative desorption of adsorbed NH_{2ad}, NH_{ad} and N_{ad} on the Co and Ni catalysts surfaces, which may be the essential reason for the higher Ea and lower TOF observed on the surfaces of Mo and Fe catalysts during thermal catalysis (Table 1).

Bimetallic catalysts (Fe-Co, Mo-Co, Fe-Ni and Mo-Ni) generally exhibit lower initial temperatures of N_2 formation compared to monometallic catalysts, with the exception of Co. Specifically, the initial N_2 desorption temperatures on Fe, Fe-Co and Co catalysts are 450 ºC, 360 ºC and 335 ºC, respectively. This suggests that combining one metal with weak metal-N binding energy (e.g., Co and Ni) and another metal with strong metal-N binding energy (e.g., Fe and Mo) results in bimetallic catalysts with moderate metal-N binding energy. Furthermore, the dominant N_2 desorption peak temperatures on Mo-Ni, Fe-Ni and Mo-Co catalysts are somewhat higher than on Fe-Co catalyst, indicating that the recombinative desorption of adsorbed NH_{2ad}, NH_{ad} and N_{ad} on Fe-Co catalyst is easier than on Mo-Ni, Fe-Ni and Mo-Co catalysts.

The NH_3 decomposition activity is not only closely related to the metal-N binding strength, but also to the adsorption strength of NH_3 molecules on the active sites. Generally, strong chemisorption of NH_3 indicates an outstanding capability of the catalysts in activating NH_3 and transforming it into adsorbed NH_{2ad}, NH_{ad} and N_{ad} species. As shown in Figure 7A, the initial temperature of NH_3 desorption from the

catalysts follows the sequence Mo < Mo-Co < Mo-Ni < Co < Fe-Ni < Fe-Co < Fe < Ni (see arrows), which suggests that the Ni, Fe, Fe-Co and Fe-Ni catalysts exhibit a relatively strong capability in adsorbing NH_3. In contrast, the Mo, Mo-Co, Mo-Ni and Co catalysts show a relative weak capability in adsorbing NH_3 molecules.

NH_3 desorption competes with NH_3 adsorption and subsequent recombinative desorption of NH_{2ad}, NH_{ad} and N_{ad}. NH_3 molecules with a weak chemisorption on the catalyst surface usually do not result in NH_3 decomposition, as they can easily desorb before further dehydrogenation and recombinative desorption can take place. In addition, it is reported that the recombinative desorption of N is the rate-limiting step in thermal catalytic NH_3 decomposition on a non-noble metal surface (Hansgen et al., 2010, Mukherjee et al., 2018, Schueth et al., 2012). The metal-N binding is too strong for N to recombine and desorb from the catalyst surface. The trade-off effect significantly influences the adsorption and desorption of N, and the trade-off between these two factors leads to an optimized catalyst (Xie et al., 2019). Therefore, only a catalyst with both a strong capability in activating NH_3 (strong chemisorption of NH_3) and a weak metal-N binding strength can exhibit excellent activity in thermal catalytic NH_3 decomposition. In brief, the Fe-Co catalyst has both a strong capability in activating NH_3 and a weak metal-N binding strength, attributed to the formation of an FeCo alloy phase. Consequently, the Fe-Co catalyst exhibits a better activity than the other seven catalysts in thermal catalytic NH_3 decomposition, as it is highly favorable for all of the adsorption, surface reaction, and desorption steps of NH_3 decomposition.

4.3 Interaction between Plasma and Catalysts

As shown in Figure 3, all catalysts exhibit synergy with plasma in NH_3 decomposition, which can be attributed to the capacity of plasma to reduce Ea and enhance TOF values (Table 1). However, the

extent of synergistic capacity, the Ea and TOF vary among the catalysts, with the Fe-Ni catalyst showing the strongest synergistic capacity, the lowest Ea and the highest TOF.

To understand why Fe-Ni performs as the most effective catalyst in plasma catalytic NH_3 decomposition, it is essential to comprehend the mechanism of plasma catalytic NH_3 decomposition. As previously reported (Huang et al., 2023), in plasma catalytic NH_3 decomposition, the NH_3 molecules are initially activated by energetic electrons, leading to excited NH_3*, NH_2 and NH species. These highly reactive species rapidly adsorb on the catalysts surface and dehydrogenate into adsorbed NH_{2ad}, NH_{ad}, H_{ad} and N_{ad} species (the adsorption step is enhanced by plasma). After that, the gas phase active species (NH_3*, NH_2 and NH) react with the adsorbed NH_{2ad}, NH_{ad}, H_{ad} and N_{ad} species through a Eley-Rideal (E-R) mechanism. Finally, the produced intermediates (e.g. N_2H_2) can easily decompose into adsorbed N_2 and H_2. In summary, the plasma accelerates the rate-limiting step (recombinative desorption of N_{ad}) through an additional reaction path (E-R mechanism) resulting from the interaction between the plasma and the catalyst. As a result, the interaction between the excited species (NH_3*, NH_2 and NH) and the catalyst surface plays a critical role in determining the activity of plasma catalytic NH_3 decomposition. Thus, we designed the following experiments to compare the interaction between catalysts and plasma.

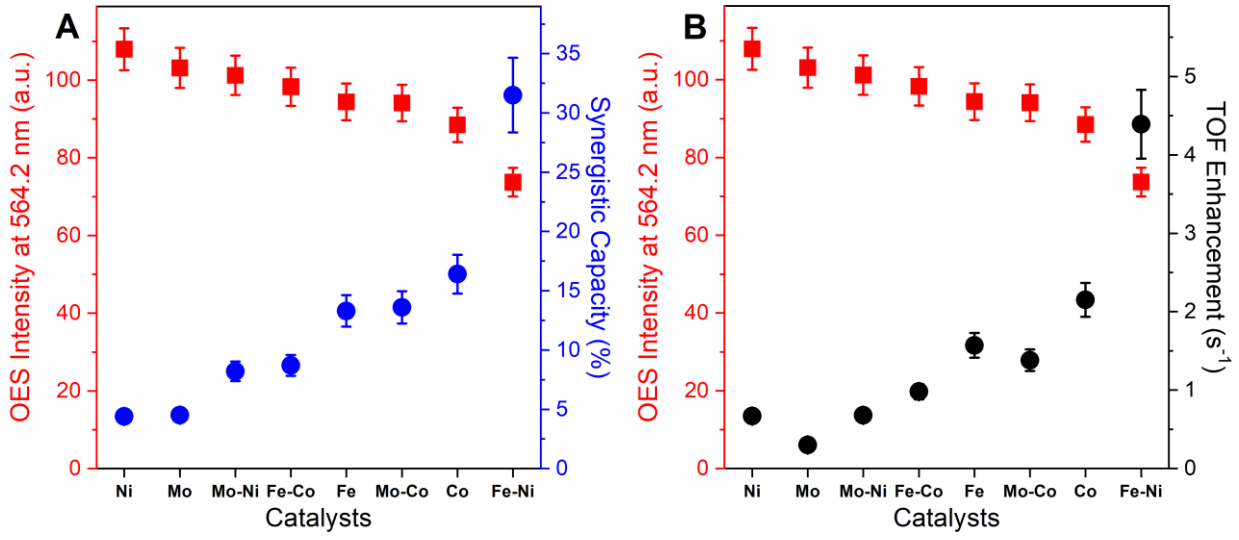

Figure 10. Correlation between the OES intensity of the NH_3 Schuster band (red squares, left axis) and the (A) synergistic capacities of the catalysts in plasma catalytic NH_3 decomposition and (B) TOF enhancement by plasma, for the various catalysts investigated.

In-situ optical emission spectroscopy (OES) was employed to diagnose the NH_3 plasma in the absence and presence of the catalyst. To ensure that the OES results were not affected by NH_3 conversion (i.e., gas composition, which can lead to different OES intensity), a lens was installed in the DBD reactor near the inlet of the feed gas (Figure S1). The distance between the head of the lens and the upper edge of plasma area was precisely fixed precisely at 4 cm. In the absence of a catalyst, molecular bands of NH_3* (564-567 nm), •NH_2 (610-670 nm and 720-780 nm) and •NH (336 nm) were observed (Figure S16) (Watson et al., 1986; Yi et al., 2019), which demonstrates that ground state NH_3 molecules were excited and dissociated in the plasma. However, in the presence of the catalysts, the OES intensity was dramatically reduced (Figure S17). This reduction was attributed not only to the shielding effect by the packed solid catalysts, but also to the adsorption of the excited species on the catalyst surface.

Figure 10 clearly illustrates that the intensity at 564 nm (i.e., the 564-567 nm band associated with the NH_3 Schuster's band) decreases in the order Ni > Mo > Mo-Ni > Fe-Co > Fe > Mo-Co > Co > Fe-Ni. The effect is somewhat more pronounced for the 5Fe-5Ni catalyst, indicating that more excited species (NH_3*, and the same applies to •NH_2 and •NH) adsorbed on the surface of the latter catalyst compared to the other catalysts. Indeed, a similar trend was observed for the intensities originating from the •NH_2 and •NH species.

Interestingly, the synergistic capacity of the catalysts follows exactly the opposite order: Ni < Mo < Mo-Ni < Fe-Co < Fe < Mo-Co < Co < Fe-Ni, as indicated in Figure 10A as well, with the most significant difference observed for the Fe-Ni catalyst. In addition, the TOF enhancement induced by plasma (i.e., TOF of plasma catalysis minus TOF of thermal catalysis) also exhibits the opposite order of the OES

intensity, except for the Ni catalyst (which may be caused by the smallest number of active sites), as shown in Figure 10B. This implies that the synergistic capacity of the catalyst is directly related to the capability of the catalyst in adsorbing reactive plasma species (either excited species or radicals). In conclusion, the stronger the capability in adsorbing reactive plasma species, the higher the synergistic capacity of the catalyst and the higher the TOF of NH_3 decomposition on the catalysts.

In summary, in NH_3 plasma, a portion of ground state NH_3 is pre-activated into highly reactive species (NH_3*, NH_2 and NH). Compared to ground state NH_3, these reactive species possess a weaker N-H bond energy and a longer N-H bond, providing a greater possibility and energy advantage to interact with the catalysts surface, which can explain the reduced Ea and enhanced TOF (Table 1). However, the question remains why the Fe-Ni catalyst exhibits more potential in adsorbing the reactive plasma species (NH_3^*, NH_2 and NH) than the other seven catalysts. In the nanoparticles of the Fe-Ni catalyst, both Fe and Ni atoms were observed (Figure 6). Typically, Fe atoms form iron nitride, showing a strong interaction with N atoms, as supported by the XRD results (Figures S6-S8) and the high temperature of N_2 desorption from the Fe catalyst surface (Figure 9). On the other hand, Ni catalysts are generally known for being excellent catalyst in hydrogenation and/or dehydrogenation reactions, due to the strong interaction between Ni atoms and H atoms. Therefore, when the Fe-Ni catalyst is exposed to NH_3 plasma, the highly reactive plasma species (NH_3^*, NH_2 and NH) can be rapidly adsorbed by the FeNi alloy particles. In other words, in plasma-catalytic NH_3 decomposition, the plasma species (NH_3, •NH_2 and •NH) can be efficiently utilized by the Fe-Ni bimetallic alloy catalysts to trigger the E-R reaction for NH_3 decomposition, although the sites were too weak for surface reactions in thermal-catalytic NH_3 decomposition, as evidenced by the challenging desorption of N_2 (Figure 9). This explains why the Fe-Ni catalyst exhibits better activity than the other catalysts in plasma-catalytic NH_3 decomposition.

4.4 Final Consideration

Plasma-catalytic NH_3 decomposition can significantly lower the reaction temperature more than 100 ^oC at the same conversion, as compared to thermal catalysis, which is attributed to the fact that reactive plasma species can regulate the catalyst surface reactions via the E-R mechanism, accelerating the reaction process. The gas reactive plasma species (NH_3*, NH_2 and NH) could easily desorb N atoms on the catalyst surface through the E-R process (Engelmann et al., 2021; Liu et al., 2022).

The characterization results reveal that the optimal catalyst for plasma-catalytic ammonia decomposition is Fe-Ni/SiO_2 (the highest NH_3 conversion) with Fe_3NiN being the active phase during the reaction. Therefore, the pure Fe_3NiN catalyst was synthesized using a nitridation process of $NiFe_2O_4$ sample (Supplementary Information), and its performance and TOF in the NH_3 decomposition reaction was evaluated. However, the Fe_3NiN catalyst shows a lower conversion and TOF value than Fe-Ni/SiO_2 catalyst (Figures S18-S20). Despite that "active component" achieves full filling within the plasma zone, which appears favorable at the microscopic scale, it is crucial to consider the electrical properties of catalysts. A higher relative dielectric constant implies a stronger ability to accumulate surface electrons in the solid material, thereby weakening the net electric field and resulting in an reduced induced electric field, especially for the supports with large ε_d values (Wang et al., 2015). The relative dielectric constant of Fe_3NiN and Fe-Ni/SiO_2 is measured to be 29.7 and 17.3, respectively. The difference in activity between Fe-Ni/SiO_2 and Fe_3NiN is indeed attributed to variations in exposed active sites and the relative dielectric constants. As a result, the performance of plasma catalysis is significantly influenced by both the loading of the active component and the electrical properties of the catalyst.

5. Conclusions

In summary, the Fe-Co bimetallic catalyst shows optimal activity in thermal catalytic NH_3 decomposition, while the Fe-Ni bimetallic catalyst exhibits the most favorable performance in plasma catalytic NH_3 decomposition. The activities of the catalysts in thermal catalysis are significantly linked

to the physicochemical properties, including particle size, metal-N binding energy, and NH_3 adsorption strength. Specifically, strong NH_3 adsorption and weak metal-N binding are found to be favorable for thermal catalytic NH_3 decomposition. Moreover, plasma catalysis involves not only the determination of the physicochemical properties of the catalysts (with particular attention to the influence of relative dielectric constant on discharge) but also their interaction with the reactive plasma species. Notably, a strong interaction with the plasma species is observed to reduce the apparent activation energy, enhance the turnover frequency of the reaction, and ultimately promote the plasma catalytic activity. These findings underscore the importance of comprehending the intricate interplay between catalyst properties and plasma interactions in catalyst design for plasma catalysis applications. In addition, this study emphasizes the need for tailored catalyst optimization based on the specific catalytic environment to achieve enhanced performance in plasma catalytic processes.

Authorship contribution statement

Shengyan Meng: Conceptualization, Data curation, Formal analysis, Writing - review & editing. **Shangkun Li**: Data curation, Formal analysis, Software. **Shuaiqi Sun**: Conceptualization, Data curation, Formal analysis, Methodology, Writing-original draft. **Annemie Bogaerts**: Formal analysis, Resources, Data curation, Writing - review & editing, Supervision, Funding acquisition. **Yi Liu**: Formal analysis, Resources, Writing - review & editing, Supervision. **Yanhui Yi**: Conceptualization, Validation, Formal analysis, Resources, Data curation, Writing - original draft, Writing - review & editing, Supervision, Funding acquisition.

Declaration of Competing Interest

The authors declare that they have no known competing financial interests or personal relationships that could have appeared to influence the work reported in this paper.

Data availability

No data was used for the research described in the article.

Acknowledgements

We acknowledge financial support from the National Natural Science Foundation of China [21503032], PetroChina Innovation Foundation [2018D-5007-0501] and the TOP research project of the Research Fund of the University of Antwerp [grant ID 32249].

Appendix A. Supplementary data

Supplementary data to this article can be found online at **XX**.

References

(1) Adamou, P.; Bellomi, S.; Hafeez, S.; Harkou, E.; Al-Salem, S.; Villa, A.; Dimitratos, N.; M anos, G.; Constantinou, A., 2023 Recent progress for hydrogen production from ammonia andh ydrous hydrazine decomposition: A review on heterogeneous catalysts. Catal. Today. https://doi.org/10.1016/j.cattod.2023.01.029.

(2) Bell, T. E.; Torrente-Murciano, L., 2016. H_2 Production via Ammonia Decomposition Using Non-Noble Metal Catalysts: A Review. Top. Catal. 59, 1438-1457. https://doi.org/10.1007/s11244-016-0653-4.

(3) Bogaerts, A.; Tu, X.; Whitehead, J. C.; Centi, G.; Lefferts, L.; Guaitella, O.; Azzolina-Jury, F.; Kim, H.-H.; Murphy, A. B.; Schneider, W. F.; Nozaki, T.; Hicks, J. C.; Rousseau, A.; Thevenet, F.; Khacef, A.; Carreon, M., 2020. The 2020 plasma catalysis roadmap. J. Phys. D : Appl. Phys 53, 443001. https://doi.org/10.1088/1361-6463/ab9048.

(4) Chen, C.; Wu, K.; Ren, H.; Zhou, C.; Luo, Y.; Lin, L.; Au, C.; Jiang, L., 2021. Ru-Based Catalysts for Ammonia Decomposition: A Mini-Review. Energy Fuels 35, 11693-11706. https://doi.org/10.1021/acs.energyfuels.1c01261.

(5) Cui, Z.; Meng, S.; Yi, Y.; Jafarzadeh, A.; Li, S.; Neyts, E. C.; Hao, Y.; Li, L.; Zhang, X.; Wang, X.; Bogaerts, A., 2022. Plasma-Catalytic Methanol Synthesis from CO_2 Hydrogenation over a Supported Cu Cluster Catalyst: Insights into the Reaction Mechanism. ACS Catal. 12, 1326-1337. https://doi.org/10.1021/acscatal.1c04678.

(6) Engelmann, Y.; van 't Veer, K.; Gorbanev, Y.; Neyts, E. C.; Schneider, W. F.; Bogaerts, A., 2021. Plasma Catalysis for Ammonia Synthesis: A Microkinetic Modeling Study on the Contributions of Eley-Rideal Reactions. ACS Sustain. Chem. Eng. 9, 13151-13163. https://doi.org/10.1021/acssuschemeng.1c02713.

(7) Fang, H.; Liu, D.; Luo, Y.; Zhou, Y.; Liang, S.; Wang, X.; Lin, B.; Jiang, L., 2022. Challenges and Opportunities of Ru-Based Catalysts toward the Synthesis and Utilization of Ammonia. ACS catal. 12, 3938-3954. https://doi.org/10.1021/acscatal.2c00090.

(9) Gu, Y.-Q.; Fu, X.-P.; Du, P.-P.; Gu, D.; Jin, Z.; Huang, Y.-Y.; Si, R.; Zheng, L.-Q.; Song, Q.-S.; Jia, C.-J.; Weidenthaler, C., 2015. In Situ X-ray Diffraction Study of Co-Al Nanocomposites as Catalysts for Ammonia Decomposition. J. Phys. Chem. C 119, 17102-17110.

https://doi.org/10.1021/acs.jpcc.5b02932.
(10) Guo, J.; Wang, P.; Wu, G.; Wu, A.; Hu, D.; Xiong, Z.; Wang, J.; Yu, P.; Chang, F.; Chen, Z.; Chen, P., 2015. Lithium Imide Synergy with 3d Transition-Metal Nitrides Leading to Unprecedented Catalytic Activities for Ammonia Decomposition. Angew. Chem., Int. Ed. 54, 2950-2954.
https://doi.org/10.1002/ange.201410773.
(11) Hansgen, D. A.; Vlachos, D. G.; Chen, J. G., 2010. Using first principles to predict bimetallic catalysts for the ammonia decomposition reaction. Nat. Chem 2, 484-489.
https://doi.org/10.1038/nchem.626.
(12) Huang, X.; Lei, K.; Mi, Y.; Fang, W.; Li, X., 2023. Recent Progress on Hydrogen Production from Ammonia Decomposition: Technical Roadmap and Catalytic Mechanism. Molecules 28 DOI: 10.3390/molecules28135245.
https://doi.org/10.3390/molecules28135245.
(13) Kirste, K. G.; McAulay, K.; Bell, T. E.; Stoian, D.; Laassiri, S.; Daisley, A.; Hargreaves, J. S. J.; Mathisen, K.; Torrente-Murciano, L., 2021. CO_x-free hydrogen production from ammonia - mimicking the activity of Ru catalysts with unsupported Co-Re alloys. Appl. Catal. B: Environ. 280, 119405.
https://doi.org/10.1016/j.apcatb.2020.119405.
(14) Kurtoglu, S. F.; Sarp, S.; Akkaya, C. Y.; Yagci, B.; Motallebzadeh, A.; Soyer-Uzun, S.; Uzun, A., 2018. CO_x-free hydrogen production from ammonia decomposition over sepiolite-supported nickel catalysts. Int. J. Hydrog. Energy 43, 9954-9968.
https://doi.org/10.1016/j.ijhydene.2018.04.057.
(15) Lendzion-Bielun, Z.; Arabczyk, W., 2013. Fused Fe-Co catalysts for hydrogen production by means of the ammonia decomposition reaction. Catal. Today 212, 215-219.
https://doi.org/10.1016/j.cattod.2012.12.014.
(16) Li, G.; Zhang, H.; Yu, X.; Lei, Z.; Yin, F.; He, X., 2022. Highly efficient Co/NC catalyst derived from ZIF-67 for hydrogen generation through ammonia decomposition. Int. J. Hydrog. Energy 47, 12882-12892.
https://doi.org/10.1016/j.ijhydene.2022.02.046.
(17) Liu, T.-W.; Gorky, F.; Carreon, M. L.; Gomez-Gualdron, D. A., 2022. Energetics of Reaction Pathways Enabled by N and H Radicals during Catalytic, Plasma-Assisted NH_3 Synthesis. ACS Sustain. Chem. Eng. 10, 2034-2051.
https://doi.org/10.1021/acssuschemeng.1c05660.
(18) Lu, A.-H.; Nitz, J.-J.; Comotti, M.; Weidenthaler, C.; Schlichte, K.; Lehmann, C. W.; Terasaki, O.; Schuth, F., 2010. Spatially and Size Selective Synthesis of Fe-Based Nanoparticles on Ordered Mesoporous Supports as Highly Active and Stable Catalysts for Ammonia Decomposition. J. Am. Chem. Soc. 132, 14152-14162.
https://doi.org/10.1021/ja105308e.
(19) Lucentini, I.; Garcia, X.; Vendrell, X.; Llorca, J., 2021. Review of the Decomposition of Ammonia to Generate Hydrogen. Ind. Eng. Chem. Res. 60, 18560-18611.
https://doi.org/10.1021/acs.iecr.1c00843.
(20) Mehta, P.; Barboun, P.; Go, D. B.; Hicks, J. C.; Schneider, W. F., 2019. Catalysis Enabled by Plasma Activation of Strong Chemical Bonds: A Review. ACS Energy Lett. 4, 1115-1133.
https://doi.org/10.1021/acsenergylett.9b00263.
(21) Meng, S.; Wu, L.; Liu, M.; Cui, Z.; Chen, Q.; Li, S.; Yan, J.; Wang, L.; Wang, X.; Qian, J.; Guo, H.; Niu, J.; Bogaerts, A.; Yi, Y., 2023. Plasma-driven CO_2 hydrogenation to CH_3OH over Fe_2O_3/γ-Al_2O_3 catalyst. AIChE J. e18154.
https://doi.org/10.1002/aic.18154.

(22) Mukherjee, S.; Devaguptapu, S. V.; Sviripa, A.; Lund, C. R. F.; Wu, G., 2018. Low-temperature ammonia decomposition catalysts for hydrogen generation. Appl. Catal. B: Environ. 226, 162-181. https://doi.org/10.1016/j.apcatb.2017.12.039.
(23) Neyts, E. C.; Ostrikov, K.; Sunkara, M. K.; Bogaerts, A., 2015. Plasma Catalysis: Synergistic Effects at the Nanoscale. Chem. Rev. 115, 13408-13446. https://doi.org/10.1021/acs.chemrev.5b00362.
(24) Qiu, Y.; Fu, E.; Gong, F.; Xiao, R., 2022. Catalyst support effect on ammonia decomposition over Ni/$MgAl_2O_4$ towards hydrogen production. Int. J. Hydrog. Energy 47, 5044-5052. https://doi.org/10.1016/j.ijhydene.2021.11.117.
(25) Schueth, F.; Palkovits, R.; Schloegl, R.; Su, D. S., 2012. Ammonia as a possible element in an energy infrastructure: catalysts for ammonia decomposition. Energy Environ. Sci. 5, 6278-6289. https://doi.org/10.1039/C2EE02865D.
(26) Silva, H.; Nielsen, M. G.; Fiordaliso, E. M.; Damsgaard, C. D.; Gundlach, C.; Kasama, T.; Chorkendorff, I. B.; Chakraborty, D., 2015. Synthesis and characterization of Fe-Ni/γ-Al_2O_3 egg-shell catalyst for H_2 generation by ammonia decomposition. Appl. Catal. A: Gen. 505, 548-556. https://doi.org/10.1016/j.apcata.2015.07.016.
(27) Simonsen, S. B.; Chakraborty, D.; Chorkendorff, I.; Dahl, S., 2012. Alloyed Ni-Fe nanoparticles as catalysts for NH_3 decomposition. Appl. Catal. A: Gen. 447, 22-31. https://doi.org/10.1016/j.apcata.2012.08.045.
(28) Srifa, A.; Okura, K.; Okanishi, T.; Muroyama, H.; Matsui, T.; Eguchi, K., 2016. CO_x-free hydrogen production via ammonia decomposition over molybdenum nitride-based catalysts. Catal. Sci. Technol. 6, 7495-7504. https://doi.org/10.1039/C6CY01566B.
(29) Sun, S.; Jiang, Q.; Zhao, D.; Cao, T.; Sha, H.; Zhang, C.; Song, H.; Da, Z., 2022. Ammonia as hydrogen carrier: Advances in ammonia decomposition catalysts for promising hydrogen production. Renew. Sust. Energ. Rev. 169, 112918. https://doi.org/10.1016/j.rser.2022.112918.
(30) Wang, L.; Yi, Y.; Guo, Y.; Zhao, Y.; Zhang, J.; Guo, H., 2017. Synergy of DBD plasma and Fe-based catalyst in NH_3 decomposition: Plasma enhancing adsorption step. Plasma Processes Polym. 14, e1600111. https://doi.org/10.1002/ppap.201600111.
(31) Wang, L.; Yi, Y.; Zhao, Y.; Zhang, R.; Zhang, J.; Guo, H., 2015. NH_3 Decomposition for H_2 Generation: Effects of Cheap Metals and Supports on Plasma-Catalyst Synergy. ACS Catal. 5, 4167-4174. https://doi.org/10.1021/acscatal.5b00728.
(32) Wang, L.; Zhao, Y.; Liu, C.; Gong, W.; Guo, H., 2013. Plasma driven ammonia decomposition on a Fe-catalyst: eliminating surface nitrogen poisoning. Chem commun. 49, 3787-3789. https://doi.org/10.1039/C3CC41301B.
(33) Wang, Y.; Fan, L.; Xu, H.; Du, X.; Xiao, H.; Qian, J.; Zhu, Y.; Tu, X.; Wang, L., 2022. Insight into the synthesis of alcohols and acids in plasma-driven conversion of CO_2 and CH_4 over copper-based catalysts. Appl. Catal. B: Environ. 315, 121583. https://doi.org/10.1016/j.apcatb.2022.121583.
(34) Wang, L.; Wang, Y. Z.; Fan, L. H.; Xu, H. L.; Liu, B. W.; Zhang, J. R.; Zhu, Y. M.; Tu, X., 2023. Direct conversion of CH_4 and CO_2 to alcohols using plasma catalysis over Cu/$Al(OH)_3$ catalysts. Chem. Eng.J. 466, 143347. https://doi.org/10.1016/j.cej.2023.143347.

(35) Watson, J. K. G.; Majewski, W. A.; Glownia, J. H., 1986. Assignment of the Schuster band of ammonia. J. Mol. Spectrosc. 115, 82-87.
https://doi.org/10.1016/0022-2852(86)90277-8.
(36) Xie, P.; Yao, Y.; Huang, Z.; Liu, Z.; Zhang, J.; Li, T.; Wang, G.; Shahbazian-Yassar, R.; Hu, L.; Wang, C., 2019. Highly efficient decomposition of ammonia using high-entropy alloy catalysts. Nat. Commun. 10, 4011.
https://doi.org/10.1038/s41467-019-11848-9.
(37) Xu, S.; Chen, H.; Fan, X., 2023. Rational design of catalysts for non-thermal plasma (NTP) catalysis: A reflective review. Catal. Today 419, 114144.
https://doi.org/10.1016/j.cattod.2023.114144.
(38) Yi, Y.; Wang, L.; Guo, Y.; Sun, S.; Guo, H., 2019. Plasma-assisted ammonia decomposition over Fe-Ni alloy catalysts for CO_x-Free hydrogen. AIChE J. 65, 691-701.
https://doi.org/10.1002/aic.16479.
(39) Zhang, D.; Cai, H.; Su, Y.; Sun, W,; Yang, D.; Ozin, G., 2022. Silica samurai: Aristocrat of energy and environmental catalysis. Chem Catal.
https://doi.org/10.1016/j.checat.2022.06.001.
(40) Zhang, H.; Gong, Q.; Ren, S.; Arshid, M. A.; Chu, W.; Chen, C., 2018. Implication of iron nitride species to enhance the catalytic activity and stability of carbon nanotubes supported Fe catalysts for carbon-free hydrogen production via low-temperature ammonia decomposition. Catal. Sci. Technol. 8, 907-915.
https://doi.org/10.1039/C7CY02270K.
(41) Zhang, J.; Mueller, J.-O.; Zheng, W.; Wang, D.; Su, D.; Schloegl, R., 2008. Individual Fe-Co alloy nanoparticles on carbon nanotubes: Structural and catalytic properties. Nano Lett. 8, 2738-2743.
https://doi.org/10.1021/nl8011984.
(42) Zheng, W.; Cotter, T. P.; Kaghazchi, P.; Jacob, T.; Frank, B.; Schlichte, K.; Zhang, W.; Su, D. S.; Schueth, F.; Schloegl, R., 2013. Experimental and Theoretical Investigation of Molybdenum Carbide and Nitride as Catalysts for Ammonia Decomposition. J. Am. Chem. Soc. 135, 3458-3464.
https://doi.org/10.1021/ja309734u.

Supplementary Information

NH_3 decomposition for H_2 production by thermal and plasma catalysis using bimetallic catalysts

Shengyan Meng[a], Shangkun Li[a], Shuaiqi Sun[a], Annemie Bogaerts[b], Yi Liu[a]*, Yanhui Yi[a]*

[a] State Key Laboratory of Fine Chemicals, School of Chemical Engineering, Dalian University of Technology, Dalian 116024, Liaoning, China.

[b] Research group PLASMANT, Department of Chemistry, University of Antwerp, Universiteitsplein 1, BE-2610 Wilrijk-Antwerp, Belgium.

* Corresponding author: Prof. Dr. Yi Liu, Prof. Dr. Yanhui Yi

E-mail address: diligenliu@dlut.edu.cn, yiyanhui@dlut.edu.cn

Content

1. Summary of the catalysts and performance

Table S1 Summary of the catalysts and performance of thermal catalysis and plasma catalysis for ammonia decomposition.

Catalyst	Temperature (°C)	Conversion (%)	H_2 production rate (mmol g^{-1} s^{-1})
Ru/SiO_2 [1]	450	36	0.19
Ru/TiO_2 [2]	500	12	0.32
Ru/ZrO_2 [3]	500	86	—
$Ni@SiO_2$ [4]	600	87	0.49
Ni/Al_2O_3 [5]	450	15	0.08
$Ni/BaTiO_3$ [6]	550	75	—
Ni/CeO_2 [7]	400	13	—
Ni/SBA-15 [8]	550	89	0.5
Ni/ZSM-5 [9]	650	98	0.55
$Fe@SiO_2$ [10]	450	8	0.5
Fe/Al_2O_3 [11]	500	25	—
Fe/SBA-15 [12]	550	18	—
$Co@SiO_2$ [13]	450	4	—
Co/Al_2O_3 [14]	500	44	0.9
$Co/MgO-Al_2O_3$ [15]	550	32	—
Mo/Al_2O_3 [16]	500	22	—
Mo/C [17]	600	66	—
Mo_2N [18]	550	94	0.4
Mo_2N [19]	550	69	—
MoS_2/laponite [20]	600	35	0.16
Fe_3C [21]	550	23	—
Co-Mo/MCM-41 [22]	500	52	—
$Fe-Mo/CeO_2-ZeO_2$ [23]	550	16	—
$Fe-Ni/TiO_2$ [24]	500	9	—
NiMoN [25]	650	100	—
$Fe-Ni/SiO_2$ (this work)	460	60	0.16

2. Experimental

1.1 Catalysts Preparation

The monometallic catalysts (Fe, Co, Ni and Mo), bimetallic catalysts (Fe-Co, Mo-Co, Fe-Ni and Mo-Ni) with 5:5 metal molar ratio, and the Fe-Co bimetallic catalysts with varying Fe/Co molar ratios were prepared using the incipient-wetness impregnation method, with fumed SiO_2 as the support. $Fe(NO_3)_3 \cdot 9H_2O$, $Ni(NO_3)_2 \cdot 6H_2O$, $Co(NO_3)_2 \cdot 6H_2O$ and $(NH_4)_2MoO_4$ were used as the precursors of Fe, Ni, Co and Mo, respectively. Before the incipient-wetness impregnation, the fumed SiO_2 support was calcined at 500 °C for 3 hours to remove adsorbed molecules (mainly H_2O and CO_2). Subsequently, metal component solution was prepared according to 10 wt.% loading (metal content) and water adsorption capacity of fumed SiO_2, before being mixed with the fumed SiO_2 support. The wet samples were standing for 8 hours before being dried in an oven at 120 °C overnight. Next, the dried sample was calcined in a furnace at 540 °C for 5 hours under an air atmosphere. Before the plasma catalytic NH_3 decomposition reaction, the calcined samples were pressed and sieved to obtain particles with diameter of 20-40 mesh. Prior to catalytic tests, the samples are reduced in a pure ammonia flow (50 mL/min NH_3) at 500 °C for 1 h.

The mixture of $Fe(NO_3)_3 \cdot 9H_2O$ (12.12 g) and $Ni(NO_3)_2 \cdot 6H_2O$ (2.908 g) with an Fe/Ni molar ratio of 3/1 was dissolved in 90 g of deionized water. Then, 10 ml of ammonia solution (25%) was added dropwise to obtain a precipitate product. The precursor solution was aged in a beaker at 90 °C in a water bath for 2 hours, followed by washing until the pH was below 8. The resulting solid product was then dried in an oven at 110 °C for 12 hours before being calcined for 5 hours to obtain $NiFe_2O_4$. The catalyst was nitrided under a pure ammonia flow, raising the temperature to 700 °C at a rate of 5 °C/min and maintaining it for 2 hours. After cooling to room temperature, the catalyst is passivated with 1% O_2/He at room temperature for 2 hours.

1.2 Activity Test

As shown in Figure S1, the hybrid plasma catalytic NH_3 decomposition was operated in a dielectric barrier discharge (DBD) reactor. The DBD reactor consisted of a glass cylinder and two coaxial electrodes. The cylinder was made of quartz glass with an inner diameter (id) of 8 mm and an outer diameter (od) of 10 mm. The quartz glass wall of the cylinder served as the dielectric barrier. A stainless-steel rod was used as the high-voltage electrode (HVE), and it was installed along the axis of the glass cylinder and connected to the AC plasma power supply (High performance plasma generators CTP-2000K). An aluminum foil, tightly wrapped on the outside of the quartz cylinder, was used as the ground

electrode (GE), and a thermocouple was connected with the GE to monitor the temperature of the reactor wall. The temperature of the catalyst bed was calibrated by FLIR equipment. A cylindrical discharge space with a length of 50 mm and a volume of 2.36 ml was formed between the HVE and GE. Before igniting the DBD, the NH_3 gas flowed through the discharge space for about 10 minutes, to make sure that air was pushed out of the reactor (for safety reasons).

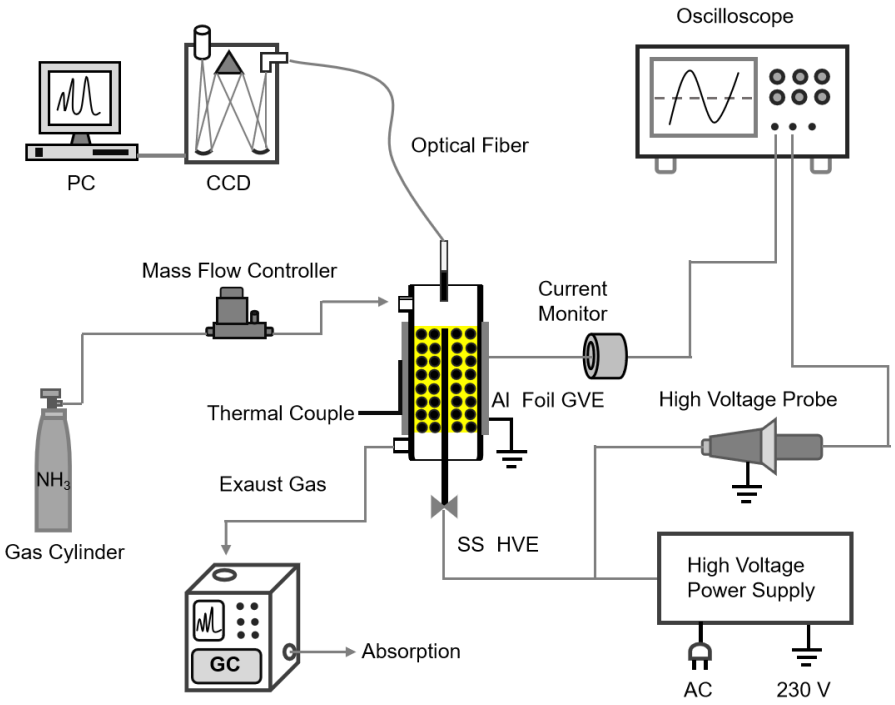

Figure S1. Schematic diagram of the experimental setup for the plasma catalytic NH_3 decomposition

The reactor was set in a tube furnace. In the case of pure plasma-driven NH_3 decomposition and plasma catalytic NH_3 decomposition, the voltage of the HVE was adjusted by the AC plasma power supply to initiate the DBD discharge. The discharge voltage, discharge current and input power were monitored on site by a digital oscilloscope (Tektronix DPO 3012) with a HV probe (Tektronix P6015A) and a current probe (Pearson 6585). The temperature of the reactor wall was in-site monitored by the thermocouple, and the temperature of the catalyst bed was calibrated using FLIR equipment (Figure S2-S3). In the case of thermal catalytic NH_3 decomposition, the reaction temperature was adjusted by the tube furnace, and it was recorded by a thermocouple too. The exhaust gas was analyzed using an on-line gas chromatograph (GC) equipped with a TCD detector. The NH_3 conversion was measured using an external standard method. During the reaction process, only H_2 and N_2 were produced, corresponding to a 100% mass balance.

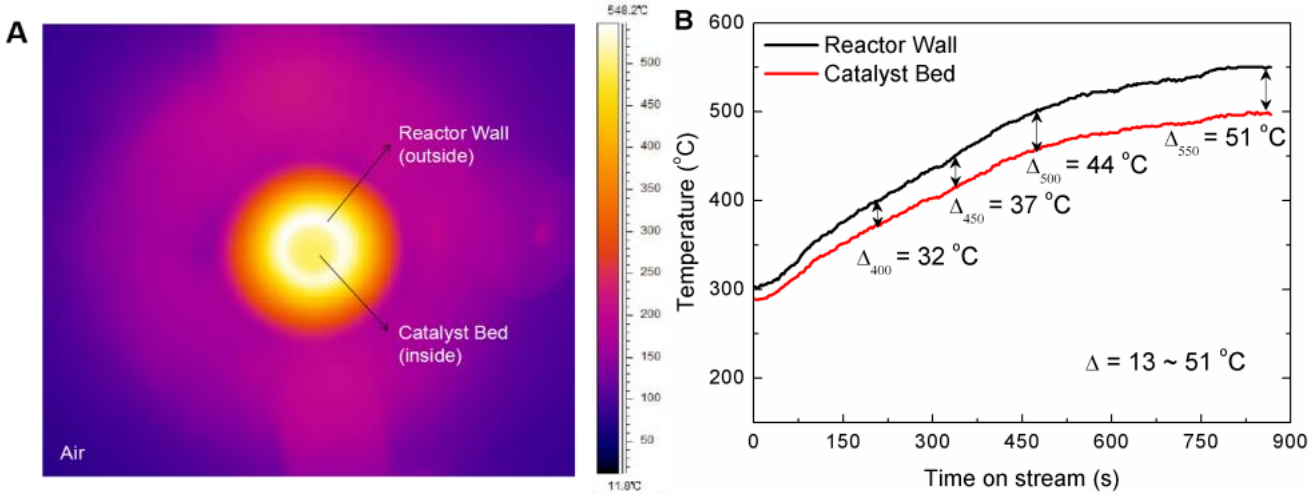

Figure S2. FLIR results of plasma catalytic NH_3 decomposition packed by a catalyst. (A) FLIR image; (B) temperature profiles.

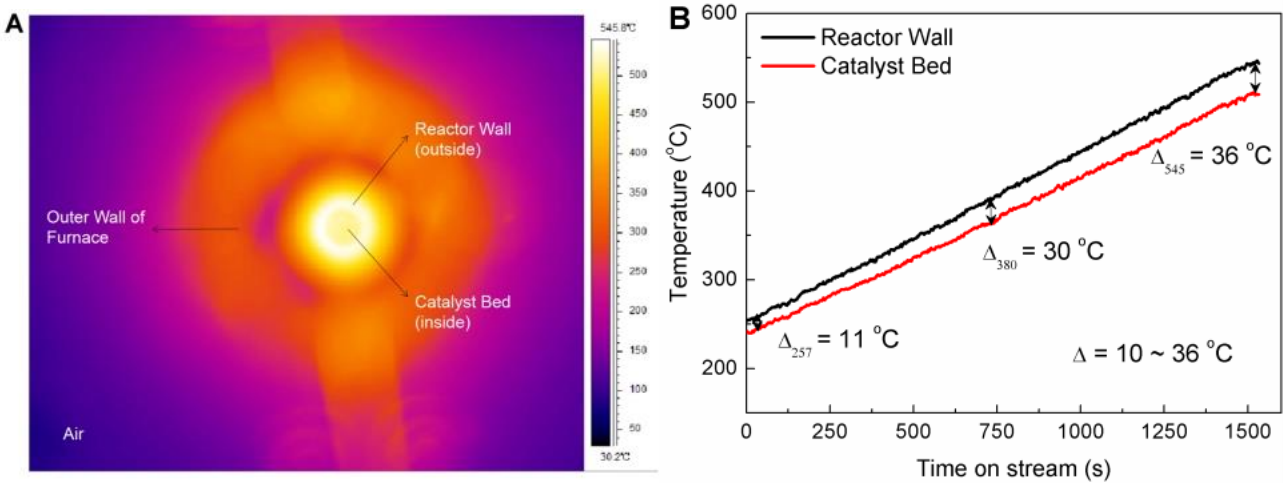

Figure S3. FLIR results of thermal catalytic NH_3 decomposition (heated by furnace) packed by a catalyst. (A) FLIR image; (B) temperature profiles.

The NH_3 conversion (X_{NH3}) is defined as equation 1, in which C_{NH3} is the moles of NH_3 converted (measured by the GC), and I_{NH3} is the moles of the inputted NH_3. The synergistic capacity between a catalyst and a DBD plasma (Q) is defined as equation 2, in which $X_{NH3(p-c)}$, $X_{NH3(p)}$ and $X_{NH3(c)}$ correspond to the NH_3 conversion in the case of "plasma + catalyst", "plasma alone" and "catalyst alone", respectively.

1.3 Catalyst Characterization

The powder XRD patterns of the samples were collected using an X-ray diffractometer (XRD, Rigaku, D-max 2400) with Cu Kα radiation. The measurement was operated at 100 mA and 40 kV, with a scanning rate of 10°/min in the range of 5-80°. The exact metal loadings were measured using an X-ray fluorescence (XRF, SRS-3400, Germany, 40 kW), which was operated at 60 kV and 150 mA. The H_2-temperature programmed reduction (H_2-TPR) was performed on a Quanta chrome ChemBET Pulsar Chemisorption instrument. Before the analysis, the samples (0.20 g) were pretreated with He from ambient temperature to 150 ºC, and kept at 150 ºC for 60 minutes. Afterward, the samples were cooled to 50 °C in He atmosphere. Finally, the H_2-TPR was carried out in a flow of H_2/Ar mixture (120 ml/min, 10％ H_2) from 100 ºC to 1000 ºC at a heating rate of 10 ºC/min. X-ray photoelectron spectroscopy (XPS) was conducted by Thermo Fisher ESCALAB XI^+ with Al Kα X-ray source. The C 1s binding energy value (284.8 eV) was taken as a reference level to calibrate binding energy. The morphology and particle size of the catalysts were examined with high resolution transmission electron microscopy (HRTEM, FEI, TF-30 device) and high-angle annular dark-field scanning transmission electron microscopy (HAADF-STEM), while energy dispersive X-ray (EDX) spectrometry was used to analyze the chemical composition of the catalysts, applying 300 kV operating voltage. The specific surface area, total pore volume, and pore diameter of the samples were measured using a nitrogen adsorption-desorption technique (Micromeritics, TriStar II physical adsorption) at -196 ºC. Before the measurement, the samples (0.1500g) were degassed at 350 ºC for 4 h. The specific surface area of the samples was calculated based on the BET approach. The total pore volume of the samples was measured at a relative pressure (P/P_0) of 0.98. The ammonia temperature programmed desorption (NH_3-TPD) of the spent catalysts were carried out using a ChemBET Pulsar Chemical Adsorbent (Quantachrome, USA), to characterize the acidity and NH_3-adsorption-desorption property. About 0.1 g sample was treated in a He atmosphere from 40 ºC to 600 ºC at a heating rate of 20 ºC/min, and was maintained at 600 ºC for 30 min; after cooling to 100 ºC, plenty of NH_3 was supplied for saturated adsorption on the surface of the spent sample; then, the sample was purged by He at 100 ºC for 90 min to eliminate physically adsorbed NH_3; at last, NH_3 desorption was examined in a He atmosphere from 100 ºC to 600 ºC at a heating rate of 20 ºC/min, and a thermal conductivity cell detector was used to detect NH_3 desorption. The exhaust gas of NH_3-TPD was collected using two tandem absorption flask, in which deionized water was placed to dissolve NH_3 desorbed from the surface of the catalysts. After that, the ammonia solution was titrated using standard hydrochloric acid solution (0.001 mol/l), and the consumption of hydrochloric acid was

used to estimate the quantity of the active sites for NH_3 chemisorption.

1.4 Plasma Diagnostics

The NH_3 plasmas (in the presence and absence of catalysts) were diagnosed using optical emission spectra (OES). The OES were collected by an ICCD spectrometer (Princeton Instruments SP 2758) in the range of 300-800 nm, using a 300 G/mm grating in the monochromator. The light emitted by the NH_3 plasma was first collected by a lens, and then directed to the monochromator by an optical fiber cable (2 meter long). In order to eliminate the effect of gas composition on the OES results, the lens was installed in the DBD reactor near the inlet of the feed gas (Figure S1), since the light emitted from other regions in the plasma was influenced by the NH_3 conversion (i.e., different gas composition yields different OES intensities). The distance between the head of the lens and the upper edge of the NH_3 plasma was fixed at ca. 4 cm. During the OES analysis, a 50 μm slit width of the spectrometer and 5 s exposure time was used.

3. Results of activity test

Table S2 NH_3 conversion and parameters in the case of "plasma alone", "catalyst alone" and "plasma + catalyst".

Plasma alone		Catalyst	**Catalyst alone**		**Plasma + catalyst**			**Synergistic capacity (%)**
P (w)	X_{NH3} (%)		T (°C)	X_{NH3} (%)	T (°C)	P (w)	X_{NH3} (%)	
29.3	3.9	Fe	360	0.5	360	29.3	7.6	3.2
34.2	8.4		405	2.2	405	34.2	16.7	6.1
38.5	11.4		440	7.1	440	38.5	28.5	10.0
41.0	14.4		460	9.9	460	41.0	37.6	13.3
30.0	4.7	Co	368	2.3	368	30.0	11.2	4.2
35.9	10.2		420	6.0	420	35.9	24.8	8.6
38.5	11.4		440	13.2	440	38.5	35.9	11.3
41.0	14.4		460	18.6	460	41.0	49.4	16.4
29.3	3.9	Ni	360	2.0	360	29.3	7.0	1.1
32.7	7.2		392	2.8	392	32.7	12.1	2.1
38.5	11.4		440	9.4	440	38.5	24.8	4.0
41.0	14.4		460	16.3	460	41.0	35.1	4.4
29.3	3.9	Mo	360	1.0	360	29.3	6.0	1.1
32.7	7.2		392	2.8	392	32.7	12.6	2.6
38.5	11.4		440	10.6	440	38.5	25.7	3.7
41.0	14.4		460	14.3	460	41.0	33.2	4.5
27.8	2.4	Fe-Co	345	4.1	345	27.8	8.5	2.0
32.2	6.7		388	8.6	388	32.2	18.5	3.2
38.3	11.4		439	15.9	439	38.3	33.6	6.3
41.0	14.4		460	21.5	460	41.0	43.5	8.7
27.3	1.9	Mo-Co	340	2.1	340	27.3	7.2	3.2
32.0	6.5		386	3.1	386	32.0	15.2	5.6
37.7	11.1		434	8.9	434	37.7	30.1	10.1
41.0	14.4		460	13.4	460	41.0	41.3	13.6
28.1	2.7	Fe-Ni	348	2.7	348	28.1	11.8	6.4
33.3	7.6		397	3.1	397	33.3	27.4	16.7
39.1	12.2		445	11.8	445	39.1	50.3	26.3
41.0	14.4		460	13.7	460	41.0	59.6	31.5
27.8	2.4	Mo-Ni	345	2.0	345	27.8	6.9	2.5
32.6	7.0		391	2.7	391	32.6	14.1	4.4
38.3	11.4		439	10.1	439	38.3	27.8	6.3
41.0	14.4		460	14.0	460	41.0	35.5	8.2

4. XRD results

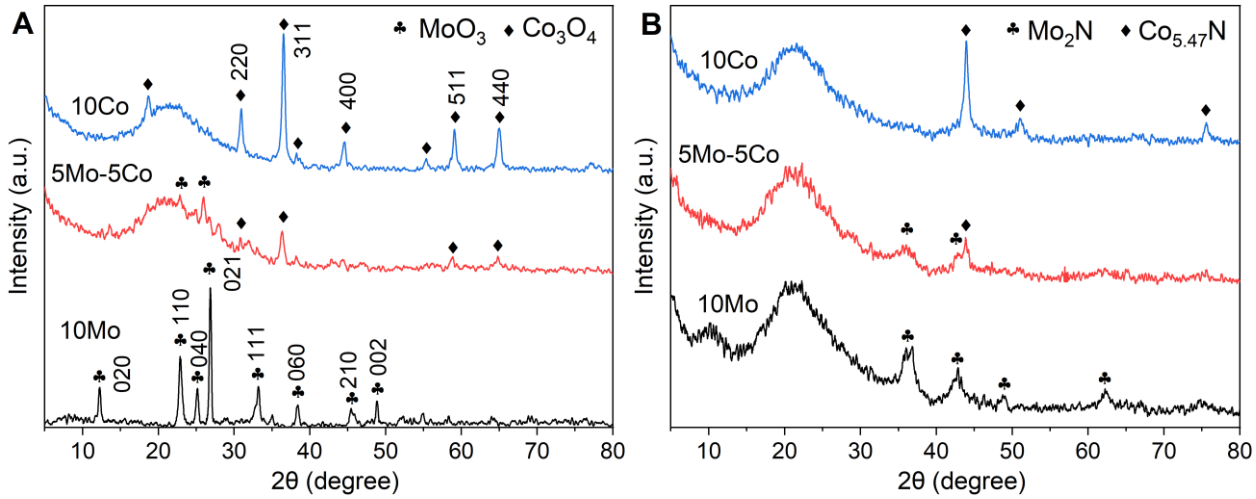

Figure S4. XRD patterns of 10Mo, 10Co and 5Mo-5Co catalysts. (A) fresh and (B) spent catalysts.

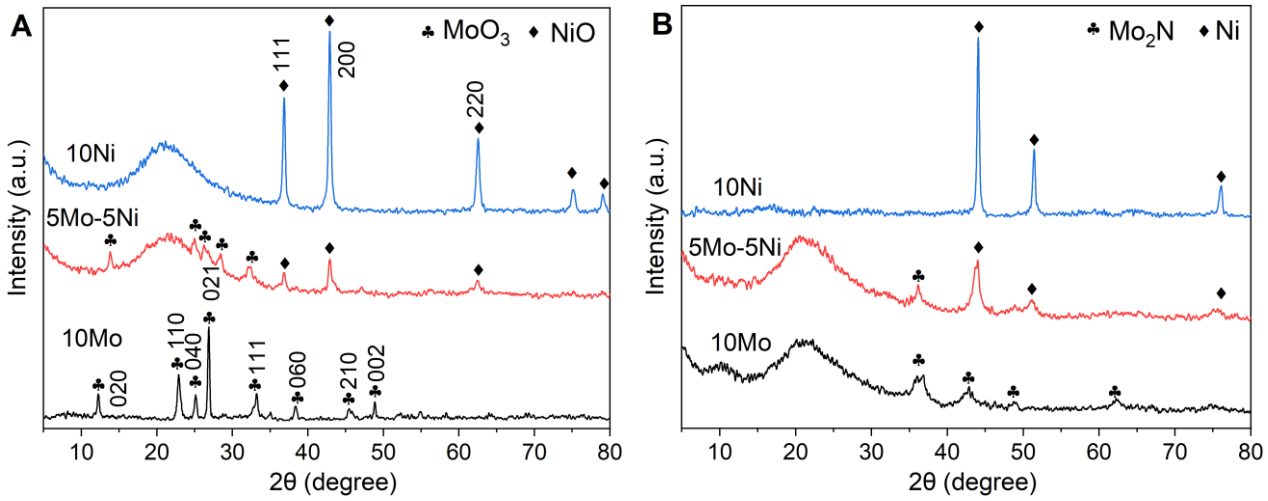

Figure S5. XRD patterns of 10Mo, 10Ni and 5Mo-5Ni catalysts. (A) fresh and (B) spent catalysts.

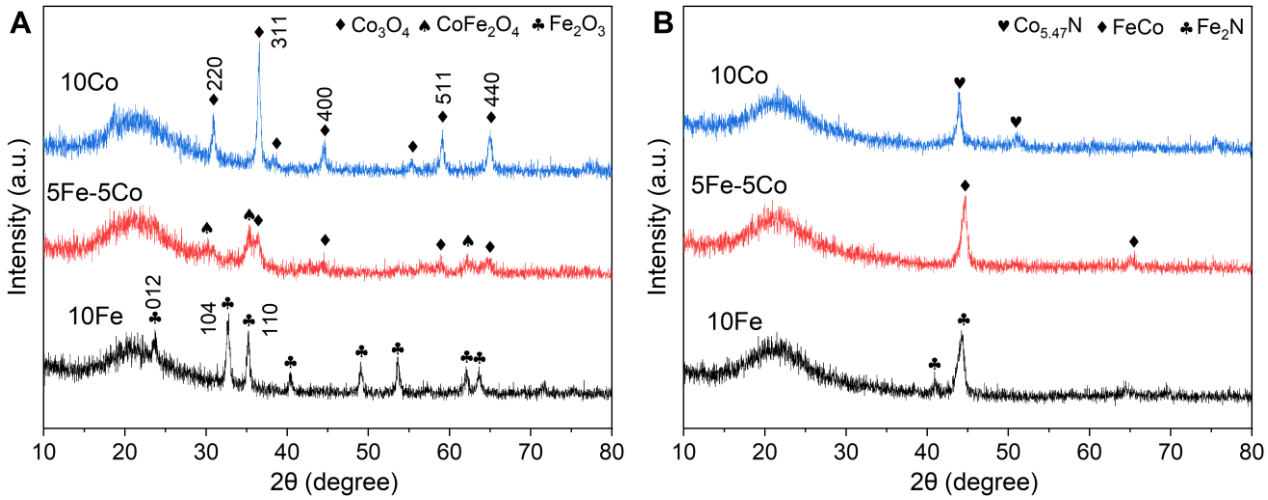

Figure S6. XRD patterns of 10Fe, 10Co and 5Fe-5Co catalysts. (A) fresh and (B) spent catalysts.

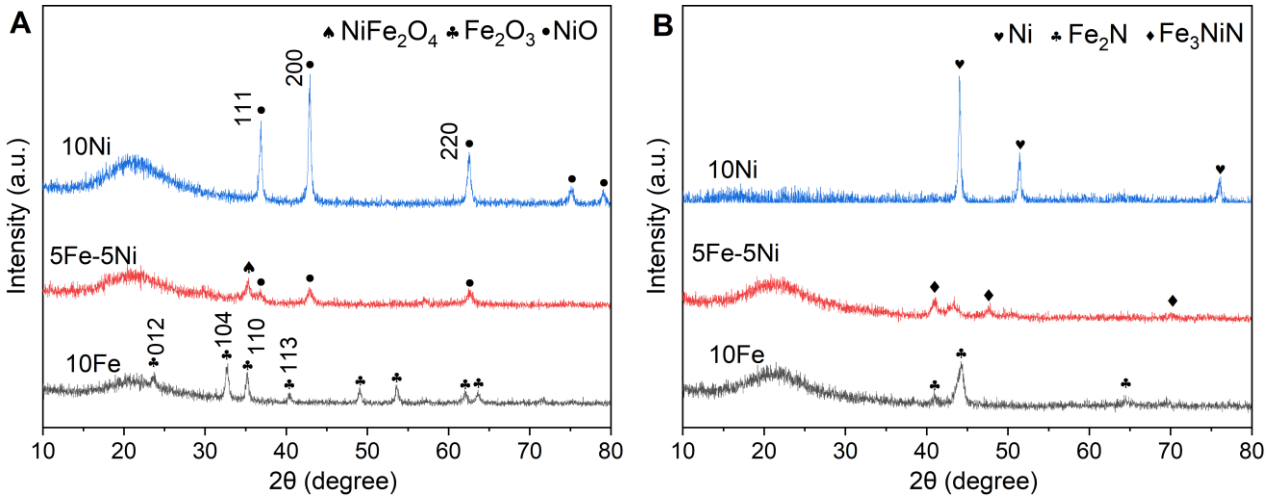

Figure S7. XRD patterns of the 10Fe, 10Ni and 5Fe-5Ni catalysts. (A) fresh and (B) spent catalysts.

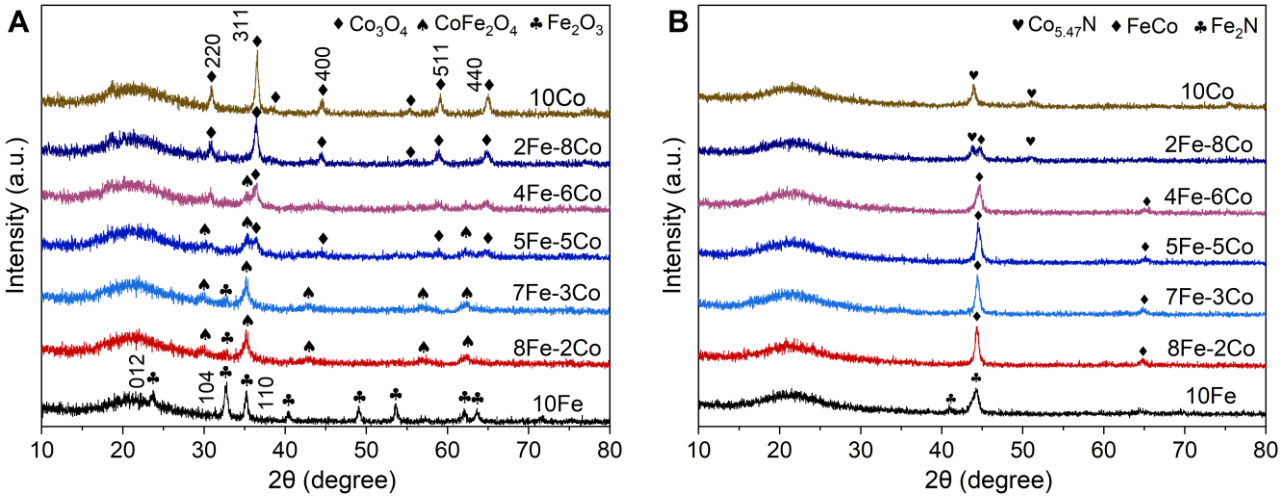

Figure S8. XRD patterns of Fe-Co bimetallic catalysts with varying Fe/Co ratio. (A) fresh and (B) spent catalysts.

5. XRF results

Table S3. X-ray fluorescence (XRF) analysis of fresh 10Fe, 10Co, 10Ni, 10Mo, 5Fe-5Co, 5Mo-5Co, 5Fe-5Ni and 5Mo-5Ni catalysts (metal oxide weight percentage content).

Catalysts	Fe_2O_3	Co_3O_4	NiO	MoO_3
10Fe	13.4%	-	-	-
10Co	-	12.6%	-	-
10Ni	-	-	12.6%	-
10Mo	-	-	-	13.8%
5Fe-5Co	6.4%	6.4%	-	-
5Mo-5Co	-	5.0%	-	9.0%
5Fe-5Ni	6.7%	-	6.3%	-
5Mo-5Ni	-	-	4.5%	8.6%

(X-ray fluorescence: SRS-3400, Germany, 40 kW, 60 kV, 150 mA, 75 mm, ±0.01°C)

Table S4. X-ray fluorescence (XRF) analysis of fresh 10Fe, 10Co, 10Ni, 10Mo, 5Fe-5Co, 5Mo-5Co, 5Fe-5Ni and 5Mo-5Ni catalysts (metal weight percentage content calculated by the data from Table S2).

Catalysts	Fe	Co	Ni	Mo
10Fe	9.8%	-	-	-
10Co	-	9.5%	-	-
10Ni	-	-	10.1%	-
10Mo	-	-	-	9.7%
5Fe-5Co	4.6%	4.8%	-	-
5Mo-5Co	-	3.8%	-	6.2%
5Fe-5Ni	4.8%	-	5.1%	-
5Mo-5Ni	-	-	3.6%	5.9%

Table S5. X-ray fluorescence (XRF) analysis of fresh Fe-Co bimetallic catalysts (Metal oxide weight percentage content).

Catalysts	Fe	Co
10Fe	13.4%	-
8Fe-2Co	11.0%	2.8%
7Fe-3Co	9.2%	3.9%
5Fe-5Co	6.4%	6.4%
4Fe-6Co	5.1%	7.6%
2Fe-8Co	2.6%	10.3%
10Co	-	12.6%

(X-ray fluorescence: SRS-3400, Germany, 40 kW, 60 kV, 150 mA, 75 mm, ±0.01°C)

Table S6. X-ray fluorescence (XRF) analysis of fresh Fe-Co bimetallic catalysts (Metal weight percentage content calculated by the data from Table S5).

Catalysts	Fe	Co
10Fe	9.8%	-
8Fe-2Co	8.0%	2.1%
7Fe-3Co	6.7%	3.0%
5Fe-5Co	4.6%	4.9%
4Fe-6Co	3.9%	5.8%
2Fe-8Co	1.9%	7.9%
10Co	-	9.6%

6. HRTEM results

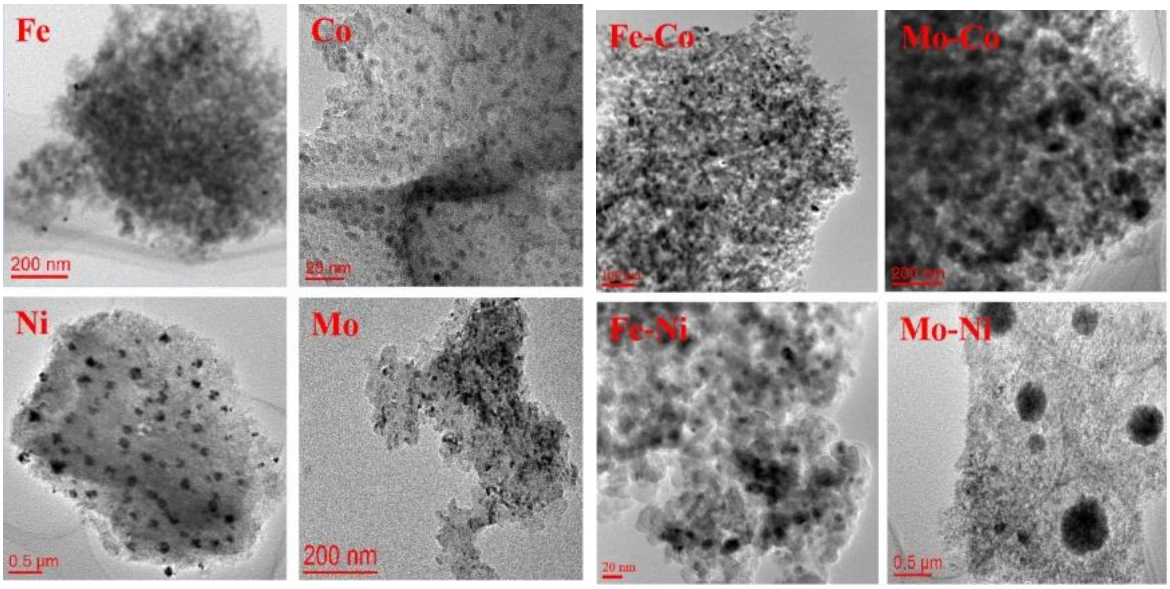

Figure S9. HRTEM images of Fe, Co, Ni, Mo, Fe-Co, Mo-Co, Fe-Ni and Mo-Ni catalysts.

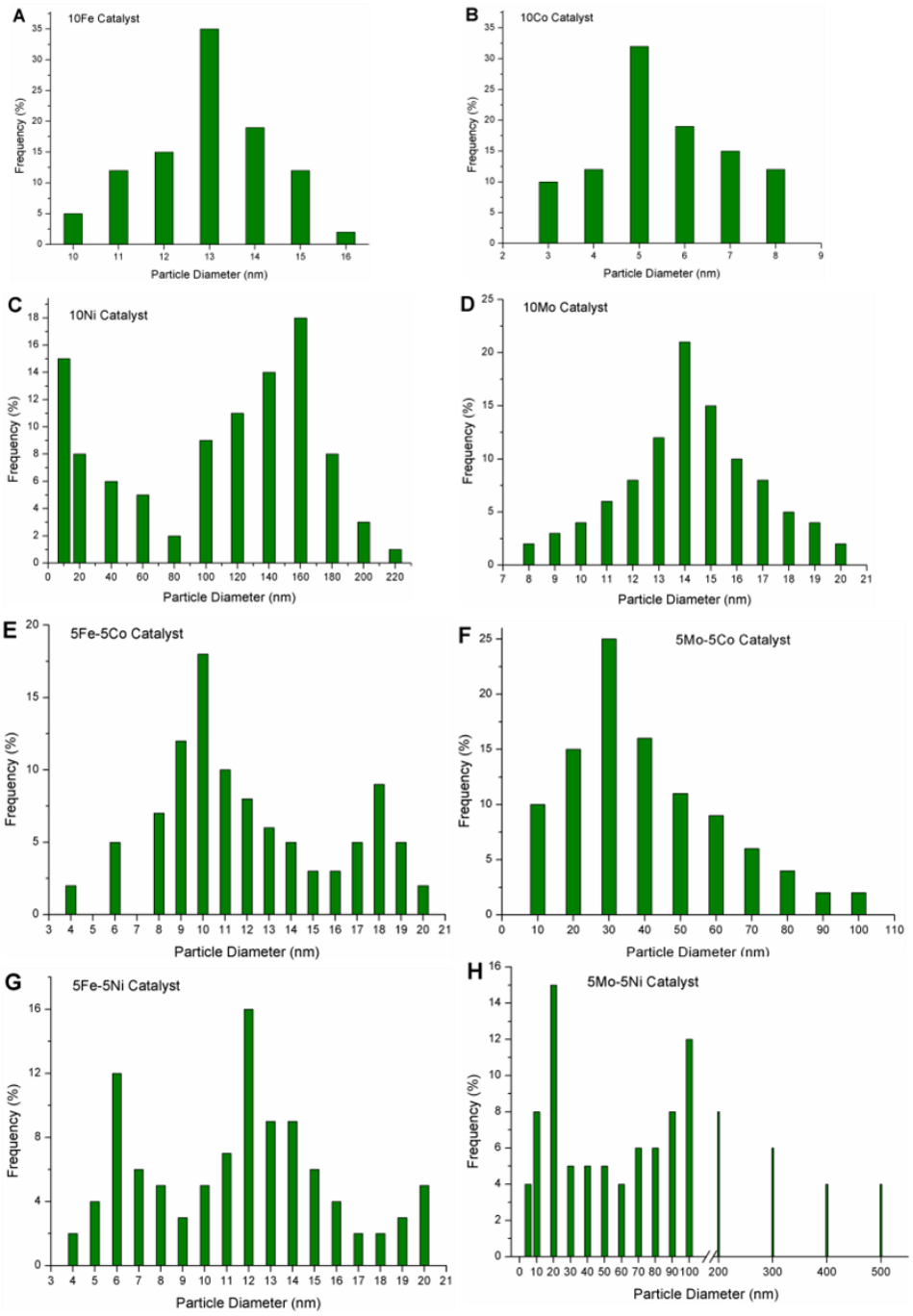

Figure S10 Particle size distribution of the catalysts derived from HRTEM images. (A) 10Fe; (B) 10Co; (C) 10Ni; (D) 10Mo; (E) 5Fe-5Co; (F) 5Mo-5Co; (G) 5Fe-5Ni; (H) 5Mo-5Ni.

7. HAADF-STEM results

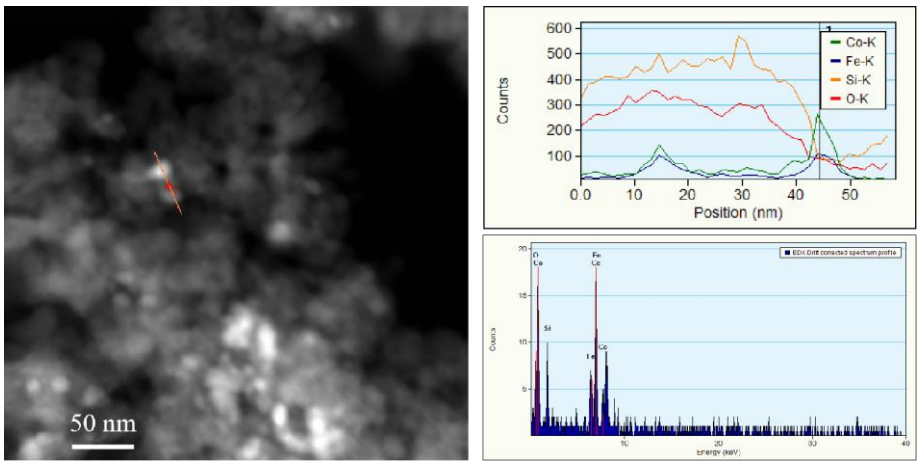

Figure S11. HAADF-STEM and EDX line scanning results of the Fe-Co catalysts.

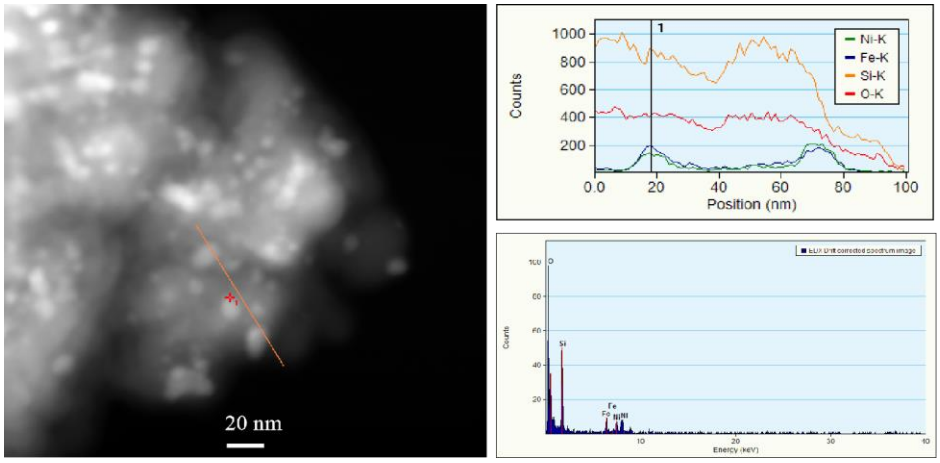

Figure S12. HAADF-STEM and EDX line scanning results of the Fe-Ni catalysts.

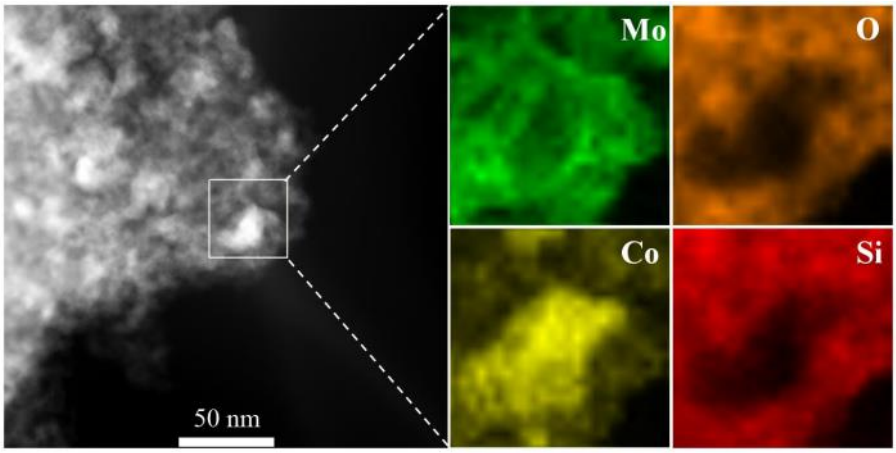

Figure S13. HAADF-STEM and EDX-Mapping images of the fresh Mo-Ni catalysts.

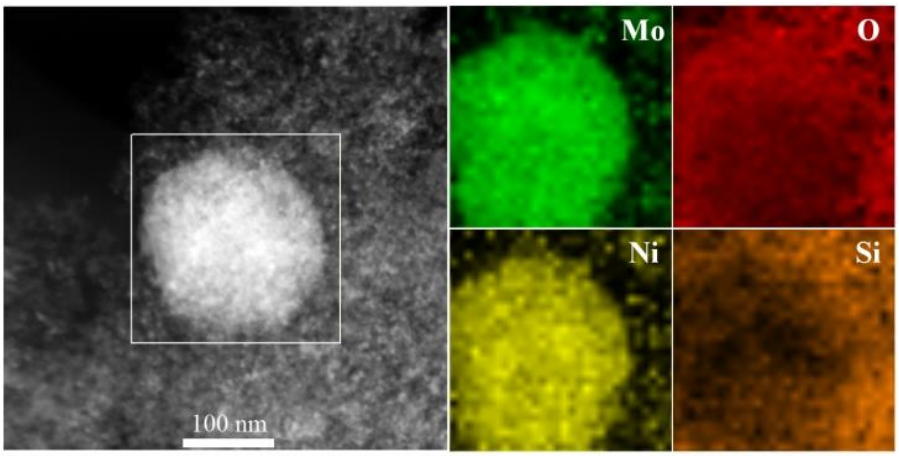

Figure S14. HAADF-STEM and EDX-Mapping images of the fresh Mo-Ni catalysts.

8. N_2-physisorption results

Table S7. BET surface area, pore volume and average pore diameter of the SiO_2 support and the catalysts.

Samples	S_{BET} (m^2/g)[a]	Pore Volume (cm^3/g)[b]	Pore Diameter (nm)
SiO_2	211.4	0.69	11.3
Fe/SiO_2	169.9	0.51	11.9
Co/SiO_2	164.6	0.52	12.5
Ni/SiO_2	168.7	0.52	12.3
Mo/SiO_2	168.1	0.52	12.4
$Fe\text{-}Co/SiO_2$	175.5	0.65	15.4
$Mo\text{-}Co/SiO_2$	173.3	0.59	14.6
$Fe\text{-}Ni/SiO_2$	182.6	0.60	13.5
$Mo\text{-}Ni/SiO_2$	173.6	0.64	15.1

[a] The BET surface area was calculated from the adsorption branch of the N_2 adsorption-desorption isotherm. [b] The pore volume was calculated from the adsorption branch of the N_2 adsorption-desorption isotherm at a relative pressure of 0.98.

Table S8. BET surface area, pore volume and average pore diameter of the SiO_2 support and $Fe\text{-}Co/SiO_2$ catalysts with varying Fe/Co ratio.

	S_{BET} (m^2/g)	Pore Volume (cm^3/g)	Pore diameter (nm)
SiO_2	211.4	0.69	11.3
$10Fe/SiO_2$	169.9	0.51	11.9
$7Fe\text{-}3Co/SiO_2$	173.3	0.59	14.6
$5Fe\text{-}5Co/SiO_2$	175.5	0.65	15.4
$4Fe\text{-}6Co/SiO_2$	173.6	0.64	15.1
$2Fe\text{-}8Co/SiO_2$	168.1	0.58	13.7
$10Co/SiO_2$	164.6	0.52	12.5

9. MS signal of H_2 during TPSR

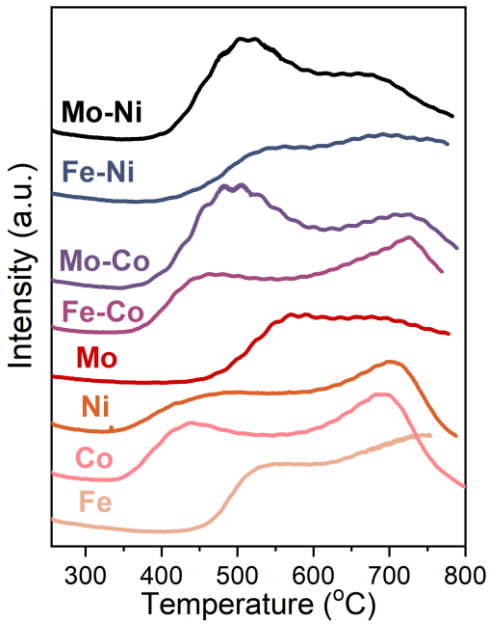

Figure S15. MS signal of H_2 during the TPSR experiments.

10. OES diagnostics results

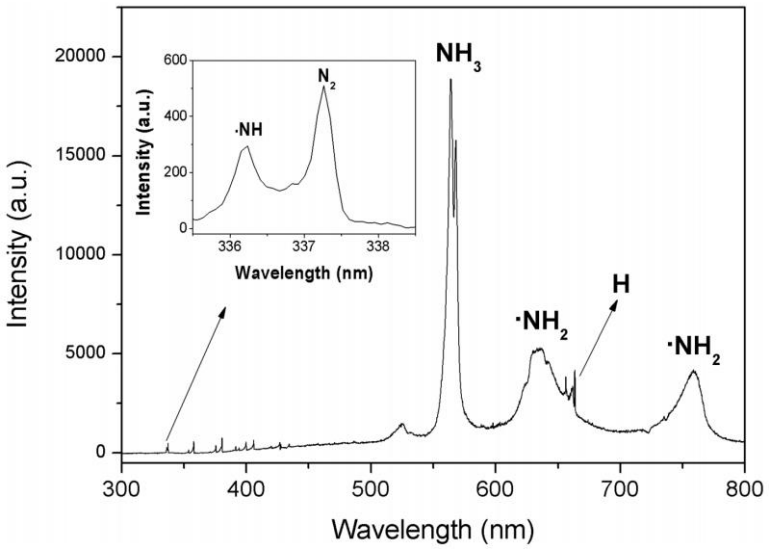

Figure S16. OES of NH_3 plasma in the absence of the catalyst (NH_3 feed rate 120 ml/min, discharge gap 3mm, discharge frequency 10kHz).

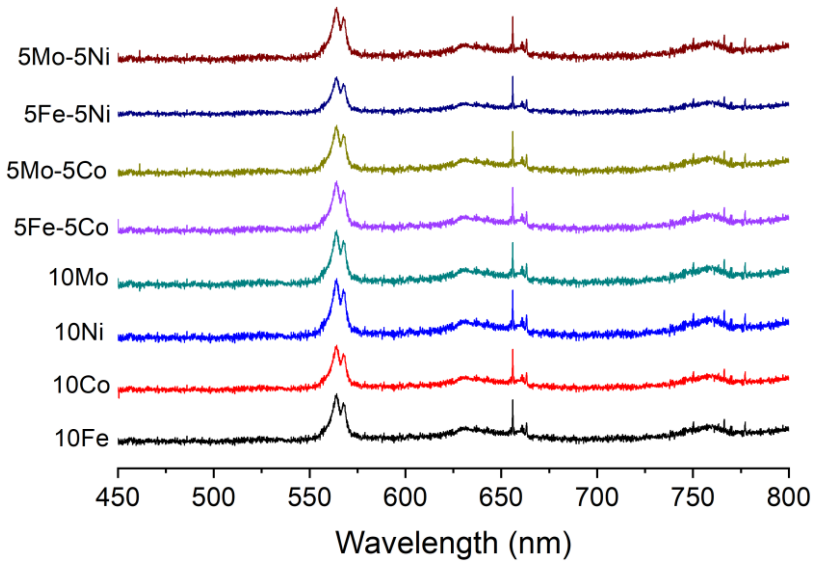

Figure S17. OES of NH_3 plasma in the presence of the catalyst. The other conditions are the same as in Figure S16.

11. In comparison to Fe_3NiN catalyst

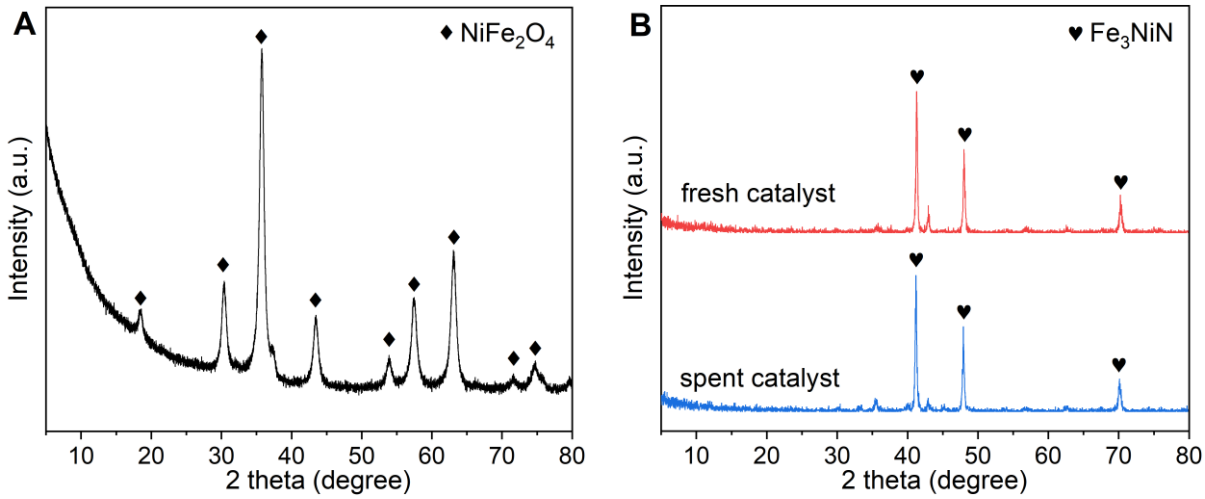

Figure S18. XRD patterns of (A) $NiFe_2O_4$ and (B) Fe_3NiN catalyst [24].

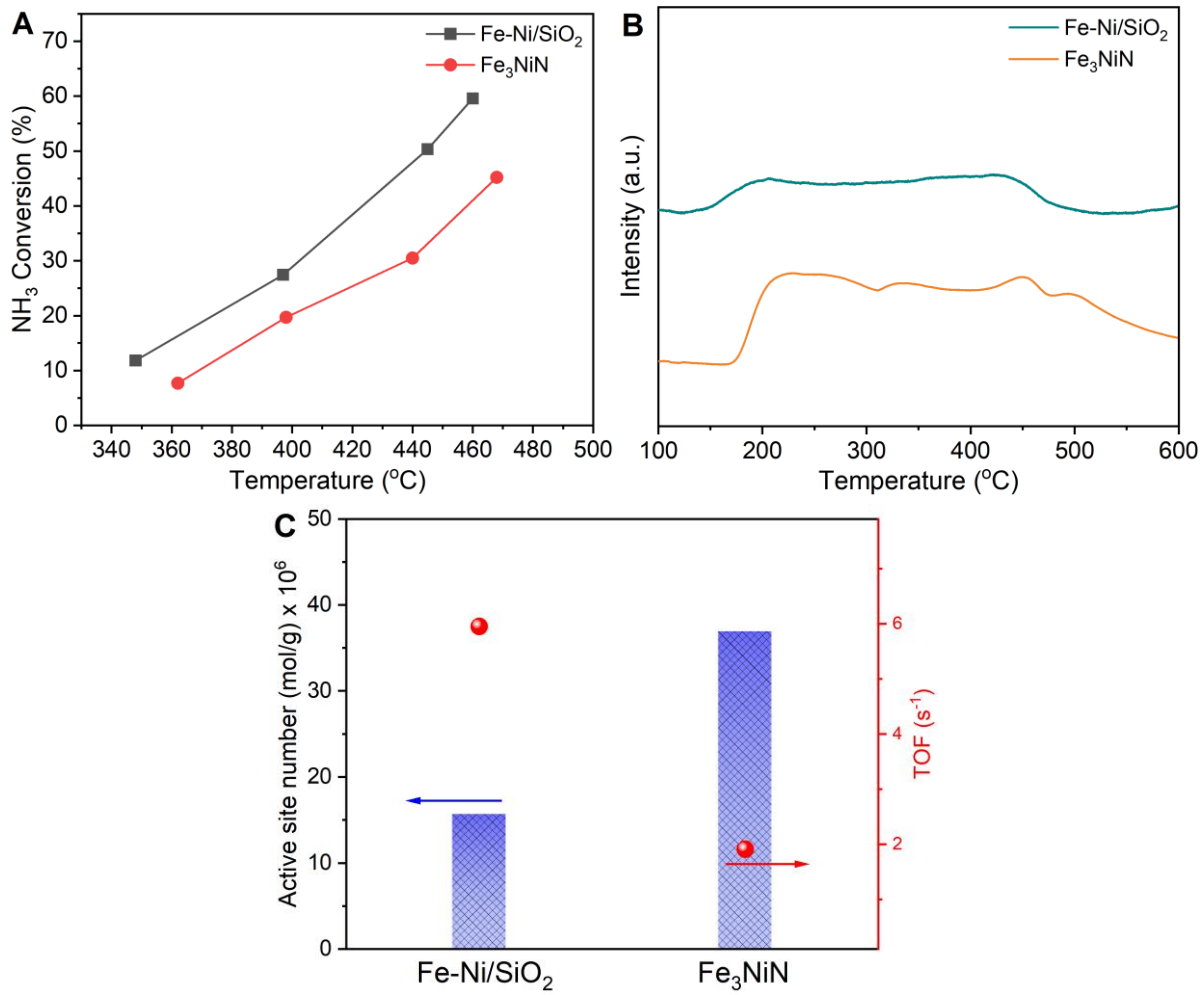

Figure S19. The Fe-Ni/SiO_2 and Fe_3NiN catalysts for (A) Results of plasma catalytic NH_3 decomposition; (B) NH_3-TPD profiles; (C) NH_3 chemisorption active site numbers and TOF.

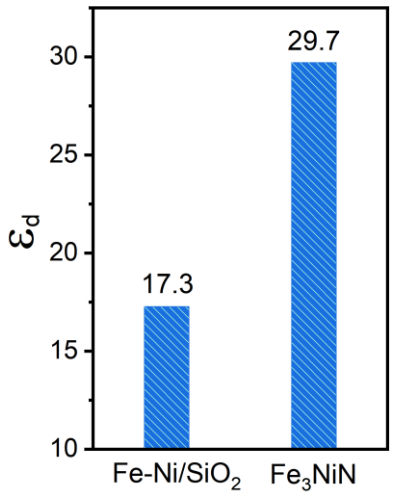

Figure S20. Relative dielectric constants of Fe-Ni/SiO_2 and Fe_3NiN catalysts.

12. References

(1) Choudhary, T. V.; Sivadinarayana, C.; Goodman, D. W., 2001. Catalytic ammonia decomposition: CO_x-free hydrogen production for fuel cell applications. Catal Letters 72, 197-201.

(2) Yin, S. F.; Zhang, Q. H.; Xu, B. Q.; Zhu, W. X.; Ng, C. F.; Au, C. T., 2004. Investigation on the catalysis of CO_x-free hydrogen generation from ammonia. J. Catal. 224, 384-396.

(3) Miyamoto, M.; Hamajima, A.; Oumi, Y.; Uemiya, S., 2018. Effect of basicity of metal doped ZrO_2 supports on hydrogen production reactions. Int. J. Hydrog. Energy 43, 730-738.

(4) Zhang, L.-F.; Li, M.; Ren, T.-Z.; Liu, X.; Yuan, Z.-Y., 2015. Ce-modified Ni nanoparticles encapsulated in SiO_2 for CO_x-free hydrogen production via ammonia decomposition. Int. J. Hydrog. Energy 40, 2648-2656.

(5) Zhang, J.; Xu, H. Y.; Jin, X. L.; Ge, Q. J.; Li, W. Z., 2005. Characterizations and activities of the nano-sized Ni/Al_2O_3 and Ni/La-Al_2O_3 catalysts for NH_3 decomposition. Appl. Catal. A: Gen. 290, 87-96.

(6) Okura, K.; Miyazaki, K.; Muroyama, H.; Matsui, T.; Eguchi, K., 2018. Ammonia decomposition over Ni catalysts supported on perovskite-type oxides for the on-site generation of hydrogen. RSC Adv. 8, 32102-32110.

(7) Li, L.; Chen, F.; Shao, J.; Dai, Y.; Ding, J.; Tang, Z., 2016. Attapulgite clay supported Ni nanoparticles encapsulated by porous silica: Thermally stable catalysts for ammonia decomposition to CO_x free hydrogen. Int. J. Hydrog. Energy 41, 21157-21165.

(8) Liu, H.; Wang, H.; Shen, J.; Sun, Y.; Liu, Z., 2008. Preparation, characterization and activities of the nano-sized Ni/SBA-15 catalyst for producing CO_x-free hydrogen from ammonia. Appl. Catal. A: Gen. 337, 138-147.

(9) Hu, Z.-P.; Weng, C.-C.; Chen, C.; Yuan, Z.-Y., 2018. Catalytic decomposition of ammonia to CO_x-free hydrogen over Ni/ZSM-5 catalysts: A comparative study of the preparation methods. Appl. Catal. A: Gen. 562, 49-57.

(10) Li, Y.; Yao, L.; Liu, S.; Zhao, J.; Ji, W.; Au, C.-T., 2011. Cs-modified iron nanoparticles encapsulated in microporous and mesoporous SiO_2 for CO_x-free H_2 production via ammonia decomposition. Catal. Today. 160, 79-86.

(11) Simonsen, S. B.; Chakraborty, D.; Chorkendorff, I.; Dahl, S., 2012. Alloyed Ni-Fe nanoparticles as catalysts for NH_3 decomposition. Appl. Catal. A: Gen. 447, 22-31.

(12) Tseng, J.-C.; Gu, D.; Pistidda, C.; Horstmann, C.; Dornheim, M.; Ternieden, J.; Weidenthaler, C., 2018. Tracking the Active Catalyst for Iron-Based Ammonia Decomposition by In Situ Synchrotron Diffraction Studies. Chemcatchem 10, 4465-4472.

(13) Yao, L. H.; Li, Y. X.; Zhao, J.; Ji, W. J.; Au, C. T., 2010. Core-shell structured nanoparticles (M@SiO_2, Al_2O_3, MgO; M=Fe, Co, Ni, Ru) and their application in CO_x-free H_2 production via NH_3 decomposition. Catal. Today. 158, 401-408.

(14) Zhang, Z.-S.; Fu, X.-P.; Wang, W.-W.; Jin, Z.; Song, Q.-S.; Jia, C.-J., 2018. Promoted porous Co_3O_4-Al_2O_3 catalysts for ammonia decomposition. Sci. China Chem. 61, 1389-1398.

(15) Podila, S.; Alhamed, Y. A.; AlZahrani, A. A.; Petrov, L. A., 2015. Hydrogen production by ammonia decomposition using Co catalyst supported on Mg mixed oxide systems. Int. J. Hydrog. Energy 40, 15411-15422.

(16) Ji, J.; Duan, X.; Qian, G.; Zhou, X.; Tong, G.; Yuan, W., 2014. Towards an efficient CoMo/γ-Al_2O_3 catalyst using metal amine metallate as an active phase precursor: Enhanced hydrogen production by ammonia decomposition. Int. J. Hydrog. Energy 39, 12490-12498.

(17) Li, L.; Chu, W.; Ding, C.; Xi, X.; Jiang, R.; Yan, J., 2017. Embedded MoN@C nanocomposites as an advanced catalyst for ammonia decomposition to CO_x-free hydrogen. Int. J. Hydrog. Energy 42, 30630-30638.

(18) Xu, J.; Yan, H.; Jin, Z.; Jia, C.-J., 2019. Facile Synthesis of Stable MO_2N Nanobelts with High Catalytic Activity for Ammonia Decomposition. Chin. J. Chem. 37, 364-372.

(19) Srifa, A.; Okura, K.; Okanishi, T.; Muroyama, H.; Matsui, T.; Eguchi, K., 2016. CO_x-free hydrogen production via ammonia decomposition over molybdenum nitride-based catalysts. Catal. Sci. Technol. 6, 7495-7504.

(20) Krishnan, P. S.; Neelaveni, M.; Tamizhdurai, P.; Mythily, M.; Mohan, S. K.; Mangesh, V. L.; Shanthi, K., 2020. CO_x-free hydrogen generation via decomposition of ammonia over al, Ti and Zr-Laponite supported MoS_2 catalysts. Int. J. Hydrog. Energy 45, 8568-8583.

(21) Kraupner, A.; Antonietti, M.; Palkovits, R.; Schlicht, K.; Giordano, C., 2010. Mesoporous Fe_3C sponges as magnetic supports and as heterogeneous catalyst. J. Mater. Chem. 20, 6019-6022.

(22) Duan, X.; Qian, G.; Zhou, X.; Chen, D.; Yuan, W., 2012. MCM-41 supported Co-Mo bimetallic catalysts for enhanced hydrogen production by ammonia decomposition. Chem. Eng. J. 207, 103-108.

(23) Lorenzut, B.; Montini, T.; Bevilacqua, M.; Fornasiero, P., 2012. FeMo-based catalysts for H_2 production by NH_3 decomposition. Appl. Catal. B: Environ. 125, 409-417.

(24) Yu, H. F.; Gadalla, A. M., 1996. Preparation of $NiFe_2O_4$ powder by spray pyrolysis of nitrate aerosols in NH_3. J. Mater. Res. 11, 663-670.